Atmos. Chem. Phys. Discuss., https://doi.org/10.5194/acp-2017-215
Manuscript under review for journal Atmos. Chem. Phys.
Discussion started: 21 June 2017

Atmospheric Chemistry and Physics Discussions

The optical, physical properties and direct radiative forcing of urban columnar aerosols in Yangtze River Delta, China

Bingliang Zhuang[1, *], Tijian Wang[1, **], Jane. Liu[1,2], Huizheng Che[3], Yong Han[1], Yu Fu[4], Shu Li[1], Min Xie[1], Mengmeng Li[1], Pulong Chen[1], Huimin Chen[1], Xiu-qun Yang[1], Jianning Sun[1]

[1] School of Atmospheric Sciences, CMA-NJU Joint Laboratory for Climate Prediction Studies, Jiangsu Collaborative Innovation Center for Climate Change, Nanjing University, Nanjing 210023, China

[2] Department of Geography and Planning, University of Toronto, Toronto, M5S 3G3, Canada

[3] Key Laboratory of Atmospheric Chemistry (LAC), Chinese Academy of Meteorological Sciences (CAMS), CMA, Beijing, 100081, China

[4] Dalian Weather Modification Office, Dalian, 116001, China

[*] Corresponding author, E-mail: blzhuang@nju.edu.cn; Tel.: +862589681156; fax: +862589683797

[**] Corresponding author, E-mail: tjwang@nju.edu.cn; Tel.: +862589683797; fax: +862589683797

Abstract: The aerosol optical and physical properties as well as its direct radiative forcing (DRF) in urban area of Nanjing (urNJ) are investigated, based on the measurements of Cimel sun-photometer combined with a radiation transfer model. We find that the annual mean 550 nm aerosol optical depth (AOD) of the total aerosols is about 0.65, dominated by scattering aerosols (about 94%), resulting in a mean single scattering albedo (SSA) of 0.93 at 550 nm and refractive index of 1.44+0.0084i at 440 nm during the sampling period. The scattering aerosol has larger size than the absorbing aerosol, with Ångström exponents (AE) of 1.19 at 440/870 nm, 0.13 smaller than the latter one. The coarse mode fraction for the scattering aerosol (18.03%) is much smaller than the absorbing aerosol's (43.91%). Thus, the fine mode aerosols presents more scattering (SSA=0.95) while the coarse aerosol is more absorption (SSA=0.82). Analysis implies that there are about 15% and 27.5% occurrences of dust and

black carbon dominated mixing aerosols, respectively, during the sampling period. All the optical properties follow a simple unimodal pattern. Aerosols in urNJ have a two-mode lognormal pattern in volume size distribution, peaking at the radius of 0.148 and 2.94 μm, and the AOD positively depends on them. Although the fine mode aerosol has a much smaller sizes than the coarse one, they have the same level of the volume concentrations (about 0.12 $\mu m^3/cm^3$) due to much higher fraction of the fine aerosol. Estimations present that the mean aerosol DRFs at the top of atmosphere (TOA) are -10.69, -16.45, +5.76 W/m^2, respectively, for the total, scattering and absorbing aerosols in clear sky. At the surface, the DRFs are 1.1-2.5 times stronger than those at TOA, and the fine aerosol DRFs in these three type of aerosols account for 83.7%, 91.7% and 67.2%, respectively, to their totals. Normally, aerosol DRFs is not very sensitive (no more than 5%) to its profiles in clear sky condition (extreme cases excepted), although both aerosol scattering and absorption could become weaker to some extent if more aerosols were in lower layers. Both the aerosol properties and DRFs have substantial seasonality.

1 Introduction

Atmospheric aerosols have significant influences on air quality, human health, and regional/global climate changes. Their loadings in the global atmosphere have increased substantially in recent years. Scientists suggested that the scattering aerosols, such as sulfate and nitrate, could greatly offset the warming effects of greenhouse gases (Kiehl and Briegleb, 1993) while the absorbing aerosols, such as black carbon (BC), might further exacerbate the global warming (Jacobson 2002). The global mean direct radiative forcings of scattering aerosols, fossil fuel BC and the total aerosols were estimated to be about -0.55, +0.2, -1.04 W/m^2, respectively (Forster et al., 2007; Reddy et al., 2005). The

atmospheric circulations and hydrological cycle would be further affected when the radiation balance is changed by the aerosols. Menon et al. (2002) suggested that changes in the trend of rainfall in China over the past 5 decades might be related to the variation of BC in southern and eastern Asia. Wang et al. (2015) indicates that the East Asia summer monsoon could become weaker due to the cooling effects of the aerosols but stronger due to the warming effects of BC.

Although many studies on the aerosol radiative forcing and climate effects have been carried out in both global and regional scales based on model simulations and observations in the past two decades (e.g., Penner et al., 2001; Bellouin et al., 2003; Liao and Seinfeld, 2005; Wu et al., 2012; Wang et al., 2015; etc.), large uncertainties still exist. Forster et al. (2007) pointed out that the global mean direct radiative forcing varied from +0.04 to -0.63 W/m^2 for the total aerosols and from +0.1 to +0.3 W/m^2 for BC. The ranges were larger in regional scales. Zhuang et al. (2013a) indicated that the simulated BC direct raidative forcing varied from +0.32 to +0.81 W/m^2 over East Asia. The uncertainties would subsequently result in large bias when assessing the aerosol climate effects. The key factors affecting the radiative forcing are the aerosol optical properties, which are related to the aerosol emissions, profiles, compositions, and mixing states (Holler et al., 2003), surface albedo and clouds (Ma and Yu, 2012; Forster et al., 2007). The uncertainties could be reduced substantially if the observed aerosol optical properties were used when calculating the forcing (Forster et al., 2007).

With the rapid increase in population and growth in economics, the trace gases and particulate matter emissions are much higher in East Asia than in the other regions (Zhang et al., 2009). Additionally, dust aerosols from northwest China and Mongolia are always transported to north and east China or even further afield (Wang et al., 2009; Sun et al., 2012; Li et al., 2015a). Consequently, aerosols in China become frequently large in loadings and complicated in compositions and spatial

distributions (Zhang et al., 2012), especially in urban agglomerations or megacities. Therefore, it is necessary to study the aerosol optical properties and radiative forcing through observation, which is premise for accurately estimating the aerosol climate effects in East Asia. Recently, substantial observation-based studies have conducted on the surface (e.g., Bergin et al., 2001; Xu et al., 2002; Zhang et al., 2004; Xia et al., 2007; Yan et al., 2008; He et al., 2009; Fan et al., 2010; Cai et al., 2011; Xu et al., 2012; Wu et al., 2012; Zhang et al., 2015; Yu et al., 2016; etc.) and columnar (e.g., Chiang et al., 2007; Pan et al., 2010; Yu et al., 2011; Zhao et al., 2013; Tao et al., 2014; Zhu et al., 2014; Che et al., 2013; 2014; 2015a, b, c; Xia et al., 2016; Zheng et al., 2016; Qi et al., 2016, etc.) aerosol optical properties and direct radiative forcing, especially on aerosols in China. For surface aerosols, the annual mean aerosol absorption coefficient (AAC) at 532 nm was about 56 Mm^{-1} in urban area of Beijing from 2005 to 2006 (He et al. 2009) and it was about 41~44 Mm^{-1} at an urban site of YRD from 2012 to 2013 (Zhuang et al., 2015). The annual mean aerosol scattering coefficients (SC) at 520 nm and AAC at 532 nm were 525 and 83 Mm^{-1}, respectively, in Xi'an in 2009 and were 456 and 96 Mm^{-1}, respectively, in Chengdu in 2011. Both AACs and SCs in urban areas are frequently stronger than those at other sites. AAC and SC were 17.5 and 174.6 Mm^{-1} in rural area of Beijing (Yan et al., 2008) and they were 6 and 158 Mm^{-1}, respectively in desert region (Xu et al., 2004). For columnar aerosols, Pan et al. (2010) shows that optical depths (AOD) at 440 nm and Ångström exponents (AE) in coastal area of the Yangtze River Delta (YRD) was about 0.74 and 1.27, respectively. Yu et al. (2011) indicates that AOD and aerosol scattering albedo (SSA) in the lake areas of the YRD exceeded 0.6 and 0.88, respectively, with significant seasonality, while in Hangzhou, they were larger than 0.72 and 0.89, respectively (Qi et al., 2016). In addition to east China, Che et al. (2011, 2013), Zhao et al. (2013), Zhu et al. (2014), Tao et al. (2014) and Yu et al. (2015) investigated the columnar aerosol optical properties in Waliguan Mt.

area, Taklimakan Desert, industrial region of northeast China, north China (which can be taken as a region with the background aerosol), the Sichuan Basin in southwest China and desert region of northwest China, respectively. In 2015, Che et al. (2015a) initiated a systematic long-term measurements of the countrywide AOD and AE in China from 2002 to 2013, including 4 remote sites, 25 rural sites, 21 urban sites. Their results showed that annual mean AOD were 0.14, 0.74 and 0.54 at the rural sites, at the urban sites, and in east China, respectively. Based on observed aerosol optical properties, the aerosol direct radiative forcing (DRF) were also estimated. Markowicz et al. (2008) found that the daytime surface DRF exceeded -20 W/m^2 in the Persian Gulf. Khatri et al. (2009) indicated that aerosols had strong ability to absorb solar radiation in Nagoya in summer, resulting in a positive DRF of +2.5 W/m^2 at the top of the atmosphere (TOA) and a strong negative forcing of -71.8 W/m^2 at the surface. Alam et al. (2011) found that aerosols could lead to a decrease in the TOA solar radiative flux, with a mean value of -22 W/m^2 in Karachi. In East Asia or China, Kuhlmann and Quaas (2010) indicated that shortwave radiation was reduced by about 25 W/m^2 due to the total aerosols over Qinghai-Tibet Plateau. Xia et al. (2016) stated that regional mean DRF in China was about -16~-37 W/m^2 at TOA and about -66 ~ -111 W/m^2 at the surface when solar zenith angle was about 60^o.

Although considerable studies on the aerosol optical properties based observations have been carried out in China, there are still gaps in the current observation network in China over YRD (one of the rapidest urbanization regions in China), especially in the urban areas of the region. To fill the gaps and to better understand the optical properties and DRF over urban areas in YRD, we investigate the aerosol optical and physical properties observed by Cimel sun photometer (CE-318, Holben et al., 1998), as well as the aerosol direct radiative forcing calculated with a radiation transfer model TUV (Madronich, 1993) combined with observed aerosol profiles and surface albedo in Nanjing. The aerosol

optical properties include: 1). the optical depths of the total, absorbing and scattering aerosols (AOD, AAOD, SAOD, respectively) and their corresponding values in fine and coarse modes (FAOD, FAAOD, FSAOD, CAOD, CAAOD, CSAOD, respectively), 2). the Ångström exponents of the total, absorbing and scattering aerosols (AE, AAE, SAE, respectively) as well as their corresponding values in fine and coarse modes (FAE, FAAE, FSAE, CAE, CAAE, CSAE, respectively), 3). single scattering albedo of the total, fine and coarse aerosols (SSA, FSSA, CSSA) and 4). refractive indexes of the aerosols. The aerosol physical properties include: 1). the volume size distributions of the aerosols, 2). The aerosol effective and mean radius as well as their volume concentrations in all, fine, and coarse modes (R_{eff}, FR_{eff}, CR_{eff}, R_{mn}, FR_{mn}, CR_{mn}, Vol, FVol, CVol, respectively).

The method is described in Section 2. Results and discussions are presented in Section 3, followed by Conclusions in Section 4.

2 Methodologies

2.1 Sampling station and instruments

The observation site (Urban Environmental Monitoring Station of Nanjing University) is located in the Gulou district, downtown area of Nanjing (32.05^{o} N, 118.78^{o} E). It is built on the roof of a 79.3 m-tall building, around which there are no higher buildings and industrial pollution sources within a 30 km radius but there are several main roads with apparent traffic pollution. The sketch map of the site (not shown) and the corresponding climatic features are available in Figure 1 of Zhu et al. (2012).

The columnar aerosol optical properties and physical characters at the site were observed using the Cimel sun photometer (CE-318, Holben et al., 1998) during the period from Apr 2011 to Feb 2014. Routine maintains and calibrations were made during the observation period. Due to the malfunctions

of the instrument and the problems of data transmission, the data from May to Sep 2012 and from Aug to Dec 2013 are invalid and excluded. The wavelength dependent optical depth (AOD) and Ångström exponents (AE) of the total aerosols were directly measured by CE-318, while the following variables are derived using the DOBVIC algorithm (Dubovik et al., 2000; 2006), including the aerosol size distributions, mode-dependent (fine and coarse) aerosol effective radius (R_{eff}), mean radius (R_{mn}), volume concentrations (Vol), wavelength dependent aerosol optical depth in fine (FAOD) and coarse (CAOD) modes, aerosol single scattering albedo (SSA) in different modes (fine and coarse), absorbing and scattering aerosol optical properties in different modes, as well as refractive indices. The DOBVIC algorithm has been used by the Aerosol Robotic Network (AERONET) and the China Aerosol Remote Sensing Network (CARSNET). Detailed descriptions on CE-318 and the corresponding observations in CARSNET are available in Li et al. (2015a) and Che et al. (2015a). For comparison, 550 nm AODs and SSAs are calculated based on given AODs at other wavelengths and AEs (Angstrom. 1929):

$$AOD_{550nm} = AOD_{440nm} \times (\frac{550_{nm}}{440_{nm}})^{-AE_{440/870nm}} \quad (1)$$

$$AAOD_{550nm} = AAOD_{440nm} \times (\frac{550_{nm}}{440_{nm}})^{-AAE_{440/870nm}} \quad (2)$$

$$SSA_{550nm} = \frac{AOD_{550nm} - AAOD_{550nm}}{AOD_{550nm}} \quad . \quad (3)$$

To make a further comparison, the concurrent observations of surface aerosol absorption coefficient (AAC) and Ångström exponents measured by a 7-channel Aethalometer (model AE-31, Magee Scientific, USA, Hansen et al., 1984; Weingartner et al., 2003 and Arnott et al., 2005) are used. Detailed calculation and correction of AAC at the site could be found in Zhuang et al. (2015). In addition, monthly mean optical depth and Ångström exponent of the total aerosols from MODIS were used to assist the analysis.

Based on observed wavelength dependent aerosol optical properties, the aerosol direct radiative forcing (DRF) in Nanjing is investigated using a radiation transfer model TUV (Madronich, 1993). The solar component of the radiative transfer scheme in TUV follows the δ-Eddington approximation. In addition to the aerosol optical properties, surface alebdo (Palancar and Toselli, 2004) and the aerosol vertical profiles (Forster et al., 2007) might also have significant influence on DRF. Thus, the wavelength dependent surface albedo from MODIS, the annual and seasonal mean aerosol profiles from CALIPSO and Polarization-Raman Lidar in Nanjing would be included when assessing the aerosol DRF in clear sky condition. The aerosol DRF in this study is defined as the difference in net shortwave radiative fluxes between including and excluding aerosol effects at TOA or at the surface. Gas absorptions in the atmosphere were set to be constant. The scattering aerosol's SSA was set to 0.9999 (similar to sulfate or nitrate, Li et al., 2015b) when calculating its DRF. DRF of the absorbing aerosols is derived from the differences between the total and the scattering aerosol DRFs.

3 Results and discussions

3.1 Optical properties of the aerosols

In this section, 550 nm optical depth, single scattering albedo and 440 nm refractive indices of the aerosols are discussed as representatives for the temporal variations and frequency distributions of these three kinds of the aerosol optical properties. In addition to the total mode aerosols, both fine and coarse ones, as well as both scattering and absorbing aerosols are also discussed. Therefore, there are altogether nine types of aerosols, including the total aerosols, total fine aerosols, total coarse aerosols, scattering aerosols, fine scattering aerosols, coarse scattering aerosols, absorbing aerosols, fine absorbing aerosols, and coarse absorbing aerosols.

Table 1 summaries the statistics of the aerosol optical properties during the study period in Nanjing. The means for the total, scattering and absorbing aerosols' optical depth (AOD) at 550 nm, averaged for the entire period, are 0.65, 0.61, and 0.04, respectively. AAOD only accounts for about 6% to the totals. Fine mode aerosol AODs (FAOD, FSAOD and FAAOD) accounts for 81.53%, 81.97% and 56.09% of the total AOD, scattering AOD (SAOD) and absorbing AOD (AAOD) in this wavelength, respectively, implying that coarse aerosols is more absorbing than the fine ones. 440/870 nm AE of the total, scattering and absorbing aerosols are about 1.20, 1.19, and 1.32, respectively. Fine aerosols have much larger AEs. FAE, FSAE and FAAE are about 0.5, 0.5 and 0.4 larger than AE, SAE and AAE, respectively. Overall, the absorbing aerosols have smaller sizes than the scattering ones in all modes, especially in coarse mode, which is consistent with the results of the surface aerosols at the site. Annual mean 470/660 AAE (from AE-31) and 450/635 nm SAE (from Nephelometer Model Aurora 3000) of the near surface aerosols are 1.58 and 1.32, respectively, at the site during the period from March 2014 to Feb 2016. The mean 550 nm SSAs are 0.93, 0.95 and 0.82 for the total, fine and coarse aerosols, respectively, further implying that the coarse aerosols have much stronger ability to absorb solar short wave radiation than the fine aerosols. Annual mean surface SSA at 550 nm for the total aerosols is little smaller (0.9) than the column one. The mean 440 nm refractive index is about 1.44+0.0084i.

Table 1

3.1.1 Seasonal variations of the aerosol optical properties

Figure 1 presents the monthly variations of 550 nm AOD (a), SAOD (b) and AAOD (c) as well as the contributions of their fine or coarse mode to the corresponding totals. Temporal variations of the

total aerosol AOD is consistent with SAOD due to significantly large ratio of SAOD/AOD. According to Zhang et al. (2009), anthropogenic emissions of trace gases and aerosols have substantially seasonal variations, low in summer but high in colder seasons especially in winter. Therefore, AODs, including the total, scattering and absorbing ones, are considerably large in winter. However, due to the effects of dust aerosols from north China in spring and moisture absorption in summer (Li et al., 2015a), AODs are also large in these two seasons. Additionally, gas to particle transformation might be more efficient in summer, which somewhat contribute to larger SAOD or FSAOD in this season. Overall, lower AODs are all found in fall for the total, scattering and absorbing aerosols. The tradeoff among anthropogenic emissions, dust aerosols, and relative humidity somewhat weakens the seasonal variations of the all mode aerosol optical depth, including AOD, SAOD and AAOD. However, the seasonalities of fine and coarse aerosol AODs are very different from and much stronger than the total mode aerosols. The largest AODs appear in spring for coarse aerosols (for both scattering and absorbing ones) while the largest AODs for fine aerosols are found in summer. The coarse aerosol AODs are lowest in summer or fall while for fine aerosol AODs, the minimum appears in spring. Owing to this, contributions of fine or coarse aerosol AODs to the totals are different among different months. The peaks of FAOD/AOD, FSAOD/SAOD, and FAAOD/AAOD appear in August, with a value of 0.96, 0.97, and 0.83, respectively, while the largest values of CAOD/AOD, CSAOD/SAOD, and CAAOD/AAOD appear in April, being 0.35, 0.32, and 0.64, respectively. The figure further suggests that the scattering or total aerosols are mostly composed by the fine particles (>80%) while the absorbing aerosols are composed, at the same level, by both fine (56%) and coarse (44%) particles in column atmosphere in Nanjing, reflecting more absorbing of the coarse aerosol than the fine one.

222 Figure 1

223

224 The aerosol Ångström exponents also have substantially seasonal variations as illustrated in
225 Figure 2, showing monthly AE, FAE, CAE, SAE, FSAE, CSAE, AAE, FAAE, and CAAE at 440/870
226 nm. Similar to AODs, the seasonality of the total aerosol AEs is similar to that for the scattering
227 aerosols. However, the seasonalities of the total and scattering aerosols is less profound than those of
228 absorbing aerosols. Both fine and coarse aerosol AEs are close to zero line in summer for scattering
229 and absorbing aerosols possibly due to the effects of high relative humidity in this season (Zhuang et al.,
230 2014a), implying that both fine and coarse mode aerosols have larger sizes in summer than in the other
231 seasons. The monthly variations of FAAE and CAAE are similar to each other, small in summer and
232 large in spring and winter, although their magnitudes are different (Figure 3). However, FSAE and
233 CSAE are strongly anti-correlated. Therefore, the seasonal variation of the total absorbing aerosol AE
234 (AAE), to some degree, agrees with that of FAAE or CAAE; its minimum appears in summer (0.74 in
235 July). However, CAAOD accounts for the most to AAOD in spring, AAE values are smaller, closer to
236 CAAE's in this season than in fall and winter. The seasonality of SAE is different from both FSAE's
237 and CSAE's; it is also different from AAE's. Under the combined effect of FSAE and CSAE, SAE
238 minimum appears in spring (0.94 in Mar) while the larger ones are found in summer and fall. Similar to
239 AAE but more, the curve of SAE would move toward the sides of CSAE in spring while toward FSAE
240 side in summer because the peaks of CSAOD/SAOD and FSAOD/SAOD appears in spring times and
241 in summer times, respectively as shown in Figure 1. The figure also indicates that the coarse scattering
242 aerosols have much larger sizes (negative values of CSAE) than the coarse absorbing aerosols,
243 suggesting that the CSAE might have much greater influence on the total SAE than CAAE on the total

AAE, although the ratio of CSAOD/SAOD is smaller than that of CAAOD/AAOD. The seasonal variations of columnar SAE and AAE are consistent with the ones of surface SAE and AAE (results not shown here).

Figure 2

In addition to AOD and AE, monthly variations of the aerosol single scattering albedo (SSA) and refractive indices are also investigated as shown in Figure 3, which shows the monthly variations of the all, fine and coarse aerosol SSA at 550 nm and the total aerosol refractive indices at 440 nm. SSA is affected by both scattering and absorbing aerosols. The fine particles are much more scattering than the coarse aerosols. Furthermore, CSSA has more significant seasonality than FSSA. The total aerosol single scattering albedo, i.e., SSA, is somewhere in between FSSA and CSSA depending on the ratios of FAOD to AOD. Overall, both FSSA and CSSA are relative smaller in summer than in the other seasons although they are considerable large in August 2011, implying that the two types of aerosols in summer are more absorbing than in the other seasons. However, SSA has a different seasonal variation from FSSA or CSSA. Due to the largest contribution of coarse aerosols in spring, SSA is the smallest in the season. The aerosol refractive indices also show substantial seasonality. The real part is large in spring but small in summer, which is similar to what was observed in Taihu Lake in the middle of YRD (Yu et al. 2011). The imaginary parts show relatively weaker seasonal variations than the real parts.

Figure 3

Table 2 summarizes the abovementioned seasonal means with the corresponding standard deviations for all the aerosol optical properties in the four seasons. Seasonal mean 550 nm AOD, SAOD and AAOD vary from 0.59 in fall to 0.75 in summer, from 0.55 in fall to 0.70 in summer, and from 0.037 in fall to 0.050 in spring, respectively. CAOD, CSAOD, CAAOD account for the majority of AOD, SAOD and AAOD in spring, with the ratios of 30.1%, 27.9%, and 58.1%, respectively. FAOD, FSAOD, FAAOD account for the majority of AOD, SAOD and AAOD in summer, with the ratios of 90.5%, 91.2% and 70.2%, respectively. As discussed above, the seasonal variations of the total mode aerosol AEs and SSA are different from the ones of fine or coarse aerosol AEs and SSA, respectively. The seasonal mean 440/870 nm AE, SAE and AAE vary from 0.99 in spring to 1.37 in fall, from 0.98 in spring to 1.38 in fall, and from 0.78 in summer to 1.50 in winter. Seasonal mean SSA, FSSA and CSSA vary from 0.920 in spring to 0.938 in winter, from 0.940 in summer to 0.956 in winter, and from 0.787 in summer to 0.834 in spring, respectively. The real part of the aerosol refractive index has relatively stronger seasonality than the imaginary part. Their largest values are all found in spring. Seasonal mean real and imaginary parts range from 1.41 in summer to 1.46 in spring and from 0.0080 in fall to 0.0084 in spring. The seasonal variation of AOD is highly inhomogeneous spatially even within the same region such as in YRD. As indicated in Che et al. (2015a), the largest AOD was found in spring while the lowest one appeared in summer in Hangzhou, east YRD. In Taihu Lake, the lowest AOD appeared in winter (Pan et al., 2010; Yu et al., 2011). The aerosols are more absorbing in winter (0.88) in Taihu Lake (Yu et al., 2011) than in spring in urban Nanjing here (0.92). However, AEs are more consistency with each other among these sites, being smallest in spring and largest in fall.

Table 2

288 **3.1.2 Frequencies of the aerosol optical properties**

289 In addition to the seasonal variations, frequency distributions of the abovementioned aerosol
290 optical properties are also investigated. Figure 4 presents the frequencies of 550 nm AOD, FAOD,
291 CAOD, SAOD, FSAOD, CSAOD, AAOD, FAAOD and CAAOD in Nanjing during the entire study
292 period. All AODs follow a near lognormal pattern. The curves of the total aerosols (Fig. 4a) are highly
293 similar to the ones of scattering aerosols (Fig b), at the same bandings, in both fine and coarse modes.
294 The peaks of the frequency curves, all exceeding 30%, appear at the values between 0.3 and 0.5, 0.2
295 and 0.4, 0.04 and 0.08 for all and scattering aerosol AODs in all, fine and coarse modes, respectively.
296 They appear at the values between 0.005 and 0.02, 0.005 and 0.015, 0.005 and 0.01 for AAOD,
297 FAAOD and CAAOD, respectively. The dominant ranges are from 0.3 to 0.9 for SAOD (AOD), 0.2 to
298 0.8 for FSAOD (SAOD) and 0.04 to 0.16 for CSAOD (CAOD), accounting for more than 83% (82%),
299 83% (82%), and 63% (67%), respectively, of the total data samples during the entire period. The
300 dominating ranges are from 0.005 to 0.06 for AAOD, 0.005 to 0.05 for FAAOD and 0.005 to 0.03 for
301 CAAOD, accounting for more than 75%, 82% and 71%, respectively, of the total data samples during
302 the entire period. The curves vary in different seasons (not shown here), shifting left-ward in low AOD
303 seasons and right-ward in high AOD seasons as suggested by Zhuang et al. (2015). In summer, the
304 curves might even have two peaks for the scattering or total aerosols, which is similar to the
305 observations in Taihu Lake (Yu et al., 2011). The frequency curve of the total AOD is much closer to
306 that of fine AOD for scattering aerosols than for absorbing aerosols because FSAOD accounts for more
307 than 82% of SAOD while FAAOD only accounts for 56% of AAOD.

308

309 Figure 4

310

311 Due to the large ratio of the scattering aerosols to the total aerosols, the frequency of the total
312 aerosol AEs resembles more that of the scattering aerosol AEs (Figures 5a and 5b). Almost all the AE
313 frequencies follow a unimodal pattern, less sharply than those of the AODs in Figure 4. The dominant
314 ranges are from 0.8 to 1.6 for SAE (AE), 1.3 to 2.1 for FSAE (FSAE) and -0.48 to -0.24 for CSAE
315 (-0.24 to -0.12 for CAE), accounting for more than 81% (83%), 83% (83%) and 82% (75%),
316 respectively, of the total data samples during the entire period. The dominant ranges are from 0.8 to 1.8
317 for AAE, 1.1 to 2.1 for FAAE and 0.6 to 1.6 for CAAE, accounting for more than 74%, 67% and 69%,
318 respectively, of the total data samples during the entire period, implying a gentler curve of AAE than
319 SAE. The frequencies of the absorbing aerosols in different modes are different from those of
320 scattering aerosols (Figure 5b and 5c). The occurrences of smaller CAAE are relatively high. The
321 values below 0.6 for CAAE account for more than 20% of the total data samples. In addition, the
322 occurrences of the large FAAE and AAE exceeding 2.5 and 2.2 reach more than 5.4% and 11%,
323 respectively, implying again that the absorbing aerosols in fine mode have a few parts of finer particles.
324 Both fine and coarse absorbing aerosols have much smaller sizes than the scattering aerosols at the
325 same modes. The frequencies of AEs also have substantial seasonality (not shown here). Comparing
326 with the annual frequency of SAE, the peak of the frequency shifts left-ward in spring, from 0.8 to 1.0,
327 but shift right-ward in fall, from 1.4 to 1.6. The frequency of AAE has a left-ward shift in summer
328 compared to the annual one, peaking at AAE values between 0.6 and 0.8.

329

330 Figure 5

331

SSAs also follow a near lognormal pattern (Figure 6a). The coarse aerosols are more absorbing than the fine aerosols (Table 1 and Figure 3). Consequently, the frequencies of SSAs peaks between 0.91 and 0.93, between 0.95 and 0.97, and between 0.80 and 0.84 for the all, fine, and coarse mode aerosols, respectively, in Nanjing during the study period. The dominant frequency appears from 0.89 to 0.97 for SSA, from 0.91 to 0.99 for FSSA, and from 0.72 to 0.92 for CSSA, accounting for more than 75%, 87% and 78%, respectively, of the total data samples during the entire study period. FSSAs concentrates more in a narrow range (from 0.89 to 0.99) than CSSA (from 0.64 to 0.96). Both real and imaginary parts of the aerosol refractive index follow a unimodal pattern and they are fairly similar to each other (Figure 6b). The frequencies peak between 1.39 and 1.42, and between 0.007 and 0.009 for the real and imaginary parts, respectively, in Nanjing during the study period. The prevailing frequency ranges from 1.36 to 1.54 for the real part and from 0.003 to 0.013 for the imaginary, accounting for more than 76% and 70% of the total data samples, respectively. The seasonality of SSA frequency (not shown) indicates that both fine and coarse aerosol SSA frequencies have a left-ward shift in summer compared to the annual one, which is opposite to the frequency of the total SSA because the fine aerosol AODs dominate, accounting for about 91% of the totals. The real part frequency in spring has a significant right-ward shift compared to that in the entire study period, peaking between 1.46 and 1.50 (not shown). The imaginary part frequency in winter has a significant left-ward shift compared to that in the study period, peaking between 0.001 and 0.003 (not shown).

Figure 6

3.1.3 Comparisons with MODIS AOD, AE and surface aerosols

AOD and AE observed by CE-318 are in reasonable agreement with those from MODIS in seasonal variation and magnitude (Figure 7). The linear correlation coefficients are 0.75 and 0.86 between CE-318 AOD and MODIS AOD and between CE-318 AE and MODIS AE, respectively. AOD at 550 nm from MODIS is larger than from CE-318, with an averaged value of 0.82 during the study period. The mean AE at 412/470 nm is about 1.43. The standard deviations of the AOD and AE are much larger from CE-318 than from MODIS.

Figure 7

The columnar AAOD and AAE from CE-318 are fairly related to the surface aerosol absorption coefficient (AAC) and AAE from AE-31 (Figure 8). However, the relationship between AAOD and AAC or between column and surface AAEs is worse than that between CE-318's and MODIS'. Although surface aerosols could be affected by transport, it is mainly from local and regional emissions and its loadings are highly related to the degree of the boundary layer development. As suggested by Zhuang et al. (2014b and 2015), surface aerosol loadings are considerably low in afternoon and summer times when the boundary layer are well developed. The columnar AAOD could additionally be affected by the upper aerosol emissions and transport in the upper atmosphere and it is less affected by the boundary height compared with the surface AAC, thus contributing a relatively worse relationship between AAOD and AAC. The surface AAE is more concentrated in a narrow range and it is larger (1.6) than that from CE-318, implying that the surface absorbing aerosols are finer thus fresher. The linear correlation coefficients are 0.39 and 0.41 between AAOD and AAC and between columnar and surface AAEs, which is slightly worse than those between FAAOD and AAC (0.46) and between columnar

376 FAAE and surface AAE (0.47).

377

378 Figure 8

379

380 Most studies on the aerosol optical properties in China mainly focus on AOD and AE in short term
381 (i.e., episodes, Che et al., 2013; Zheng et al., 2016; Che et al., 2015b). Studies on annual (Yu et al.,
382 2011) and decadal (Che et al., 2015a) scales have been carried out in recent years based on CE-318
383 measurements. Che et al. (2015a) indicated that long tern averages of the total aerosol optical depth at
384 440 nm and Ångström exponent at 440/870 nm in urban areas were about 0.75 and 1.05 in north China,
385 0.98 and 1.09 in Sichuan Basin, 0.78 and 1.36 in Pearl River Delta region (PRD), 0.65 and 1.0 in
386 northeast China, 0.66 and 89 in northwest China, 0.92 and 1.0 in central China, 0.9 and 1.25 in coastal
387 areas of YRD. AOD at 440 nm in urban Nanjing averaged over the study period is about 0.84, which is
388 larger than that in north China, northwest China, northeast China, and PRD but smaller than that in
389 coastal cities of YRD and about the same as the one in HeFei (0.84). Aerosols in northwest China,
390 central China, north China have larger sizes (smaller AE) than those in Nanjing. AE in the cities and at
391 rural areas within YRD is at a similar magnitude. Che et al. (2015a) further suggested that the aerosols
392 in urban areas likely had larger AODs and AEs than those in mountain and desert areas, so did in
393 Nanjing. Qi et al. (2016) presents that the aerosol single scattering albedo at 440 nm in Hangzhou, east
394 YRD is about 0.90, 0.92 and 0.70 for the total, fine and coarse aerosols, respectively, also implying that
395 the coarse aerosols are more absorbing than the fine ones. Our measurements show similar results to Qi
396 et al. (2016) for Hangzhou. However, aerosols in Nanjing are more scattering than in Hangzhou in both
397 fine and coarse modes.

398

399 **3.2 Physical properties of the aerosols**

400 In addition to the optical properties, the aerosol physical properties including volume size
401 distributions, mode dependent sizes (radius) and volume concentrations are also retrieved. Figure 9
402 shows the volume size distributions of the aerosols in different seasons (Figure 9a) and in different
403 AOD levels (Figure 9b) in Nanjing. Aerosols in Nanjing have a typical bimodal structure in volume
404 size distribution in all seasons, presenting a two-mode lognormal distribution: fine mode (radius < 0.6
405 μm) and coarse mode (radius > 0.6 μm). The annual peaks appear at the radius of 0.148 μm in fine
406 mode and 2.94 μm in coarse mode. Similar to the aerosol optical properties, aerosol volume size
407 distribution also has substantial seasonality. The peak in spring is much lower in fine mode and higher
408 in coarse mode than that in the other seasons due to the effect of dusts which results in a left-ward shift
409 in the distribution in fine mode. Therefore, the mean radius of the aerosols increases significantly in
410 spring due to a high proportion of coarse particles, leading to smaller AE. In summer, the curve has a
411 right-ward shift, showing an increase in both fine and coarse aerosol sizes due to high levels of
412 moisture in the season. The fine particles dominate in summer and result in large AE, opposite to what
413 is in spring. In Nanjing, the aerosol volume size distribution varies with different AOD values (Figure
414 9b). Overall, the peaks likely shift right-ward with increasing AOD for fine aerosols but left-ward for
415 coarse aerosols. The peaks are at the radii of 0.113 and 3.857 μm when AOD is below 0.2 and at 0.194
416 and 2.94 μm when AOD exceeds 1.4. Additionally, AOD show a positive dependence on the volume
417 concentrations of both fine and coarse aerosols. The AOD in Nanjing could be evenly affected by both
418 fine and coarse aerosols when AOD is considerably large or relatively small. High levels of AOD (>1.4)
419 are attributed to the coarse aerosols in spring and to the fine aerosols in summer. AOD values ranging

420 from 1.0 to 1.4 is more resulted from the fine particles. The results here are rather consistent with the
421 ones in Yu et al. (2011), Qi et al. (2016), and Zheng et al. (2016).
422
423 Figure 9
424
425 The seasonal variation in the aerosol effective and mean radius, and volume concentrations in
426 Nanjing are presented in Figure 10. The mean effective radius are about 0.34, 0.16, and 2.18 μm for the
427 total, fine and coarse aerosols, respectively, during the study period. The mean averaged radius are
428 about 0.80, 0.19, and 2.67 μm for the total, fine and coarse aerosols, respectively. The seasonal
429 variation of the aerosol effective radius resembles that of the mean radius in all the modes. Both fine
430 and coarse aerosol radius are larger in summer than in the other seasons due to the moisture absorption
431 growth of the aerosols. With seasonal variations in the proportion of fine or coarse aerosols in the total,
432 the radius of the total aerosols are much larger in spring than in the other seasons. The seasonal
433 variations of the radius in all modes anti-correlate well with the corresponding aerosol AEs as shown in
434 Figure 2. The mean volume concentrations are 0.24, 0.11 and 0.13 $\mu m^3/cm^3$ for the total, fine and
435 coarse aerosols during the study period. Overall, both fine and coarse aerosols evenly contribute to the
436 total aerosol volume in Nanjing, similar to what is found in Hangzhou (Qi et al., 2016). The coarse
437 aerosols contribute slightly more to the total aerosol volume concentrations because of its high
438 proportions in spring (Figure 10b). The seasonality of the volume concentrations in fine and coarse
439 aerosols are different, although the seasonality of their radius are similar to each other, because the
440 volume also depends on the concentrations of the aerosols. The highest volume concentrations appear
441 in spring for the coarse aerosols and in summer the for fine aerosols. As expected, the seasonal

variation of the total aerosol volume is affected by both fine and coarse aerosols.

Figure 10

3.3 Aerosol classification based on its optical properties

The aerosol types could be identified based on the relationships between SSA at 491 nm and AE at 491/870 nm, real refractive index at 670 nm and AE at 491/870 nm, as well as between SSA differences (dSSA=SSA_{870nm}-SSA_{491nm}) and AE at 491/870 nm (Russell et al., 2014) as shown in Figure 11. Russell et al. (2014) indicated that: 1. The polluted dust aerosols have smaller AE (near 1.0), relatively smaller SSA levels (0.85 to 0.95), but much larger real refractive index (1.45 to 1.55) and SSA differences (0 to 0.05) compared with other aerosols. 2. The aerosols from the developing urban have smaller sizes than the polluted dust (AE ranging from 1 to 1.6), but they have larger SSA (0.9 to 1.0), smaller real refractive index (1.4 to 1.5) and SSA differences (around 0). 3. The aerosols from the urban dominated by Industrial (UrbInd) or from biomass burning have the largest AE (exceeding 1.6). However, the UrbInd aerosols have much larger SSA and SSA differences while smaller real refractive index compared with biomass burning aerosols. If there were two kind of aerosols having nearly identical coordinates, further information is needed. Based on the classification standards, the Figure 11 presents that aerosols in urban area of Nanjing could be effected by the long distant transported dust (or polluted dust) substantially in spring times. And in rest seasons, the aerosols are mostly from the local emissions and they belong to the developing urban aerosols. It is a pity that the observations missed a biomass burning event in Jun 2012 (Zhuang et al., 2014b, 2015) when the instrument was maintained. It's a very serious biomass burning episode, which directly results in extremely high BC surface concentrations

(6-7 times to the annual means, Zhuang et al., 2014b). Figure 11 would be more comprehensive if this event were captured.

Figure 11

In addition to the types, the aerosol mixtures/compositions could also be identified based on SSA and AAOD. Generally, dust and biomass burning aerosol SSAs would increase and decrease with wavelength, respectively. Non-monotonically changes in SSA with the wavelength might be due to the other type aerosol dominated mixtures as indicated by Li et al. (2015c), who then proposed two curvature parameters defined as the second derivative of the second-order polynomial fit of SSA and wavelength and the fit of AAOD and wavelength as shown in Eq. 4 and Eq. 5 to provide additional information on the aerosol compositions.

$$\ln(SSA_\lambda) = \beta_2 \ln(\lambda)^2 + \beta_1 \ln(\lambda) + \beta_0 \quad (4)$$

$$\ln(AAOD_\lambda) = \alpha_2 \ln(\lambda)^2 + \alpha_1 \ln(\lambda) + \alpha_0 \quad (5)$$

Where, $-\beta_2$ and α_2 are the SSA Curvature and AADO Curvature, respectively. Detailed statements could be found in Li et al. (2015c). Based on these parameters, the aerosols could basically be identified as the dust dominated, black carbon (including biomass burning and urban/industrial aerosols) dominated and other mixed (peak) type aerosols. The former two type of aerosols have monotonically increase and decrease SSA spectral shapes, respectively. The SSA or AAOD Curvature is mostly concentrated at or around 0 for the BC dominated aerosol mixture, which is much smaller than that of dust dominated aerosol mixtures (0.1 for SSA Curvature and 0.5-1 for AAOD Curvature) (Li et al., 2015c). Our observations show the similar results as shown in Figure 12, further implying

that aerosols in urban Nanjing could be effected by the long distant transported dust as indicated in Figure 11 and could also be affected by biomass burning or the industrial emissions. The results additionally suggested that there are about 15% (mostly appearing in Spring) and 27.5% (mostly being in Fall and Winter) occurrence of dust dominated and BC dominated mixing aerosols, respectively, in urban areas of Nanjing during the observed period.

Figure 12

In May 2011, Nanjing was affected by a very strong dust storm from northwest China and Mongolia (Li et al., 2015a), the mean SSA and AAOD Curvatures in 1st May 2011 were as large as 0.12 and 1.11, respectively, which is close to the values (0.11 and 1.24, respectively) of the pure dust aerosol (Li et al., 2015c). Both SSA and AADO Curvatures have substantial seasonality, larger in colder seasons (not shown here).

3.4 The direct radiative forcing of the aerosols

Basing on abovementioned wavelength dependent optical properties and combining with the observed surface albedo and aerosol profiles, the total, scattering and absorbing aerosol direct radiative forcing (DRF) in all, fine and coarse modes at both TOA and the surface in Nanjing using are investigated using a radiation transfer model TUV (Madronich, 1993), under clear sky condition. The scattering aerosol's SSA is assumed to be equal to that of sulfate or nitrate, which is about 0.9999 (Li et al., 2015b) when assessing its DRF. The absorbing aerosol DRF was derived from the difference between the total aerosol and scattering aerosol DRFs because of lacking the observed SSA of the

mixed absorbing aerosol. DRFs based on AAODs, AAEs and black carbon (BC) SSA (Li et al., 2015b) is also calculated to make a comparison with the absorbing aerosol DRFs.

Figure 13 shows the mean vertical profiles of the aerosols observed by CALIPSO and Polarization-Raman Lidar in Nanjing. To make a comparison, profiles in the figure have been standardized to the percentage (%). The aerosols mainly concentrate below 4 km, accounting for about 61% and 88% according to CALIPSO and Lidar, respectively, suggesting that differences exist between CALIPSO and Lidar derived profiles and the vertical aerosols from the Lidar distribute much more at the lower troposphere. Thus, a combined profile simply assumed to be averaged from CALIPSO and Lidar (gray line) is additionally included. It indicates that aerosols account for about 75% of the totals below 4 km and about 60% in the boundary layer for the combined profile, which to some extent is similar to the default profile of TUV (Palancar and Toselli, 2004). The aerosol DRFs are all estimated by TUV using these profiles.

Figure 13

3.4.1 The aerosol direct radiative forcing in both clear and cloudy sky conditions

DRFs, unless otherwise specified, hereinafter all represent the averaged values among CALIPSO, Lidar and combined profile based forcing. Figure 14 shows the seasonal mean daytime TOA and surface DRFs of the total, scattering and absorbing aerosols in all, fine and coarse modes in clear sky conditions in Nanjing. The scattering aerosol could exert a negative forcing both at TOA and the surface while the absorbing aerosol exerts a positive forcing at TOA and a negative forcing at the surface.

530 Both the scattering and absorbing aerosol DRFs have significant seasonality. The strongest
531 (weakest) forcing at TOA appears in summer (spring) for fine scattering aerosols and in spring
532 (summer) for coarse scattering aerosols. The fine scattering aerosol AOD is about one order of
533 magnitude larger than the coarse one, directly resulting in its much stronger DRFs. In addition to
534 SAODs, surface albedo could also lead to changes in the aerosol DRFs. In a bright surface, the
535 scattering aerosol DRFs might decrease in the condition with fixed loadings or AODs (Zhuang et al.,
536 2014a). The seasonal mean surface albedo averaged from four wavelengths (440, 670, 870 and 1020
537 nm) are about 0.145, 0.170, 0.129, and 0.137 in spring, summer, fall, and winter, respectively, implying
538 that the scattering aerosol DRFs, to some extent, are weakened in spring and summer due to the higher
539 surface albedo. The strongest DRF for the total scattering aerosols is found in summer, orderly
540 followed by that in winter, spring and fall due to the co-affections of SAODs and surface albedo,
541 although SAOD in spring is higher than that in winter. The seasonal variations in the surface scattering
542 aerosol DRFs are consistent with those at TOA.

543 Similar to the scattering aerosols, the TOA DRFs of the absorbing aerosols are the strongest in
544 summer for fine mode and in spring for coarse mode when the aerosol AODs are the highest in the
545 corresponding seasons. However, the TOA DRFs are relatively weaker in winter for fine absorbing
546 aerosols and in summer and winter for coarse absorbing aerosols. Different from the scattering aerosols,
547 the coarse absorbing aerosol DRFs have the same orders of magnitude as the fine ones. DRFs of
548 absorbing aerosols are also affected by both the AAODs and surface albedo to a certain degree. Zhuang
549 et al. (2014a) stated that higher surface albedo would considerably lead to stronger TOA DRFs and
550 weaker surface DRFs for absorbing aerosols with fixed loadings or AAODs, which is different from the
551 scattering aerosols. Additionally, the solar zenith angle also plays a considerable role in intensifying

552 DRFs. For example, at 8 and 9 pm on 13th Aug in 2011, AAODs and AAEs are all equal to 0.23 and
553 1.18, respectively. However, the corresponding DRFs are 3.37 and 4.69 W/m^2 at TOA and -9.12 and
554 -10.03 W/m^2 at the surface under a condition of the same SSA, surface albedo and aerosol profiles,
555 implying that the DRFs would be stronger in warmer seasons or at noon when the optical properties of
556 absorbing aerosols and the other affecting factors are fixed. Thus, a stronger TOA DRF of the fine
557 absorbing aerosols in spring than in winter might be related to higher surface albedo and solar zenith
558 angles, although their AAODs in winter are substantially higher. Both fine and coarse absorbing
559 aerosol DRFs at TOA are stronger in fall than in winter possibly owing to higher solar zenith angles in
560 fall. The all mode absorbing aerosol DRFs at TOA also have different seasonality from the scattering
561 aerosols, being the strongest in spring, orderly followed by those in summer, fall and winter. The
562 seasonal variations of the absorbing aerosol DRFs at the surface are somewhat different from at TOA in
563 fine and coarse modes. The weakest surface DRF appears in spring for fine absorbing aerosols and in
564 summer for coarse absorbing aerosols possibly due to a higher surface albedo in this season as
565 suggested by Zhuang et al. (2014a). The surface DRFs of the all mode absorbing aerosols are also the
566 strongest in spring due to the combined effects of the corresponding fine and coarse aerosols.

567 The absorbing aerosols can considerably offset the negative DRFs of the scattering aerosols at
568 TOA and strengthen the positive DRFs of the scattering aerosols at the surface (Figures 14a and 14d).
569 Thus, the weakest and strongest TOA DRFs of the total fine aerosols appear in spring and winter,
570 respectively. The total coarse aerosol DRFs in summer are positive at TOA due to a high proportion of
571 absorbing aerosol to the totals (smaller SSA as showed in Figure 3a). For all modes, the seasonal
572 variation of the total aerosol DRFs at TOA are more consistent with that of the fine mode, and the
573 DRFs are all weaker than the ones of scattering aerosols. The surface DRFs of the total fine aerosols

574 are strongest in summer while the weakest in spring, which is opposite to the total coarse aerosols. Due
575 to the co-affection of fine and coarse aerosols, the total DRFs of all mode aerosols at the surface are the
576 strongest in summer and weakest in fall. The existence of cloud would reduce the solar radiation
577 reaching the surface or lower atmosphere, thus affecting the aerosol DRFs, including their levels and
578 seasonality. This issue would be further addressed in the further.
579
580 Figure 14
581
582 Due to lack of the observed SSAs, the absorbing aerosol DRFs here are mainly estimated from the
583 difference between the total and scattering aerosol DRFs. Additionally, DRFs based on observed
584 AAOD, AAE and fresh BC SSA (Li et al., 2015b) are also accessed to investigate the differences
585 between these two types of DRFs as shown in Figure 15. Although the absorbing aerosol DRFs are
586 estimated in different ways, they are highly correlated at both TOA and the surface, implying that they
587 have the same seasonality. However, the DRFs from the second method are much weaker than that
588 from the first one, implying that the DRFs from these two methods might represent different mixing
589 states of the absorbing aerosols. Apparently, the second none represents the forcing of fresh absorbing
590 aerosols while the DRFs from the former one might represent the forcing of the aged or internally
591 mixed absorbing aerosols. Jacobson (2000) suggests that the aged absorbing aerosols have much
592 stronger ability to absorb solar radiation, with a factor of two. Zhuang et al. (2013a and 2013b) stated
593 that the regional mean TOA DRFs over East Asia is about +1.56 W/m^2 for internally mixed BC and
594 about +0.81 W/m^2 for externally mixed BC. Comparison here further prove the importance of the
595 mixing states to estimate the absorbing aerosol direct radiative forcing.

596

597 Figure 15

598

599 Table 3 lists the annual mean clear sky DRFs of the total, scattering and absorbing aerosols in all,
600 fine and coarse modes at TOA and the surface in Nanjing. The DRFs at the surface are all stronger than
601 those at TOA. The mean DRFs are -10.69, -16.45, 5.76 W/m^2 at TOA and -25.54, -21.37 and -8.38
602 W/m^2 at the surface for the total, scattering and absorbing aerosols, respectively. The TOA DRFs in
603 fine mode are nearly an order of magnitude stronger than those in coarse mode for the total and
604 scattering aerosols. The DRFs of the fine absorbing aerosols have the same orders of magnitude as, but
605 stronger than those of the coarse absorbing aerosols.

606 Table 3

607

608 Various studies on the aerosol DRFs have been carried out based on observations or numerical
609 models. Forster et al. (2007) summarized the global mean clear and cloudy sky DRFs of the total
610 aerosols from observations, which are -5.4 and -0.55 W/m^2, respectively. Using a regional climate
611 chemistry model, RegCCMS, Zhuang et al. (2013a and 2013b) estimated the regional mean DRFs of
612 the total and BC aerosols over East Asia and they are -4.97 and +1.2 W/m^2, respectively, in clear sky.
613 On a sub-regional or urban scale, Markowicz et al. (2008) found that the daytime surface DRF
614 exceeded -20 W/m^2 in Persian Gulf. Khatri et al. (2009) indicated that aerosols exerted a positive DRF
615 of +2.5 W/m^2 at TOA and a strong negative forcing of -71.8 W/m^2 at the surface in Nagoya in summer.
616 Alam et al. (2011) found that total aerosol DRFs at TOA was about -22 W/m^2 in Karachi. In East Asia
617 or China, Wang et al. (2009) reported that the TOA DRFs of total aerosols in Beijing are -2, -21 and -16

618 W/m^2 on clear, haze, and fog days, respectively. Kuhlmann and Quaas (2010) indicated that the total
619 aerosol DRFs was about -25 W/m^2 over Qinghai-Tibet Plateau. Che et al. (2015c) indicated that the
620 daytime total aerosol DRFs in northeast China was about -16.82 W/m^2. Che et al. (2014) also reported
621 that the TOA DRFs of the total aerosols in north China Plain exceeded -30 and -40 W/m^2 in rural and
622 urban areas, respectively, during the period with serious haze-fog episodes. Xia et al. (2016) pointed
623 out that the regional mean DRF in China was about -16~-37 W/m^2 at TOA and about -66 ~ -111 W/m^2
624 at the surface when solar zenith angle was about 60^o. Over all, the DRFs of urban aerosols are much
625 stronger than those on the regional or global scale. Our results show the same orders of magnitude of
626 DRFs as those for other regions in earlier studies.
627
628 **3.4.2 The aerosol direct radiative forcing varies in different aerosol profiles**
629 Different aerosol profiles might result in different DRFs. Figure 16 presents the TOA and surface
630 DRFs of the total, scattering and absorbing aerosols based on four kinds of aerosol profiles from
631 CALIPSO, Lidar, Combined CALIPSO and /Lidar shown in Figure 13 as well as the default one in
632 TUV (Palancar and Toselli, 2004) in clear sky condition. The figure shows that the aerosol direct
633 raidative forcing in clear sky condition is not very sensitive to the aerosol profiles, although the
634 differences among absorbing aerosol TOA-DRFs from different profiles are more obvious to some
635 degree than the scattering aerosol DRFs or the surface forcing. Here, a profile impact factor: PIF is
636 defined as the ratio of the standard deviations among the four types of DRFs in Figure 16 to the
637 averaged values among these four DRFs. The PIF is about 4.97% for absorbing aerosol TOA-DRF
638 while below 2% for the rest types of DRFs during the study period. Overall, both the scattering and
639 absorbing aerosol DRFs at TOA would become weaker to some extent if more aerosols were

640 concentrated in lower layers of atmosphere or within boundary layer especially for the absorptions,
641 implying that the aerosol profiles might also become significant in some extreme cases (high level of
642 aerosol appearing very low layers in serious pollution episodes). The aerosol profiles might have much
643 more influence on the DRFs in cloudy sky condition because the absorbing aerosols over brighter cloud
644 would absorb more short wave radiation (Podgorny and Ramanathan, 2001). This issue is also going to
645 be addressed in the further.
646
647 Figure 16
648
649 Although the DRFs of the total, scattering and absorbing aerosols, as well as their sensitivities to
650 the aerosol profiles are analyzed in this study, there still exist limitations to be addressed in the future.
651 First, the absorbing aerosol DRFs are estimated from the difference between the total and scattering
652 aerosol DRFs. The methods are still with uncertainties to some extent. Therefore, the observed SSA of
653 the absorbing aerosols is needed in further studies to enhance the accuracy. Second, the uncertainty can
654 be further reduced if data with higher temporal resolutions of the aerosols profiles are used to substitute
655 their annual means. Third, long-term trends of the aerosol optical properties and direct radiative forcing,
656 including their interannual and interdecadal variations, should be taken into consideration. Finally,
657 extremely high aerosol loadings are frequently observed in serious pollution episodes, including dust
658 storms, biomass burning, and regional transport (Zhuang et al., 2014a, b and 2015). The aerosol optical
659 and physical properties as well as the radiative forcing would be rather different in these extreme
660 episodes, which also deserve further studies.
661

4 Conclusions

In this study, the aerosol optical and physical properties observed by Cimel sun photometer (CE-318), as well as its direct radiative forcing (DRF) calculated by a radiation transfer model TUV based on observed aerosol optical properties, profiles, and surface albedo in urban area of Nanjing are investigated.

The annual mean aerosol optical depths at 550 nm are 0.65, 0.61, and 0.04 for the total (AOD), scattering (SAOD) and absorbing (AAOD) aerosols, respectively. The fine mode fractions of the total, scattering and absorbing aerosols are 81.53%, 81.97% and 56.09%, respectively. The absorbing aerosols are finer, with an Ångström exponent (AE) of 1.32 at 440/870 nm, 0.13 (0.12) larger than the scattering (total) aerosols. Fine aerosol AEs are much larger than coarse one, especially for scattering aerosols. Additionally, the fine aerosol is more scattering (SSA=0.95) while the coarse aerosol more absorption (SSA=0.82). The mean 440 nm refractive index is about 1.44+0.0084i during the study period. AOD and AE observed by CE-318 are rather similar to those from MODIS. AAOD and AAE from CE-318 to some extent are related to the surface aerosol absorption coefficient (AAC) and AAE. The aerosols in Nanjing have smaller AOD than, but the same AE as, and are more scattering than, those in coastal cities of YRD.

The aerosol optical properties have significant seasonality. AOD and AE of scattering aerosols are lowest in fall and in spring while highest in summer and fall, respectively. The highest AAOD and AAE appear in spring and winter while the lowest ones are found in fall and summer. Fine mode AOD are all at maximum in summer but minimum in spring, while coarse AOD are at maximum in spring. The AEs in both fine and coarse modes are closer to zero in summer than those in the other seasons due to the effects of high humidity. The total aerosol AOD and AE seasonality is consistent with the

scattering aerosols. However, the smallest SSA is found in spring, although both FSSA and CSSA are relative smaller in summer. All AODs and SSAs follow a near lognormal pattern and almost all of the AE and refractive indices follow a unimodal pattern. The ranges around their means dominated, accounting for at least 60% to their total data samples during the entire study period. They also have substantial seasonality.

The aerosols in Nanjing have a two-mode lognormal pattern in volume size distribution, with substantial seasonality, peaking at the radius of 0.148 and 2.94 μm in annual scale. The fine (coarse) mode peak has a leftward (rightward) shift relative to the annual peaks in spring while both of them have a right-ward shift in summer. AOD show a positive dependence on the volume concentrations in both fine and coarse modes. The peaks would be close to each other with increasing AOD. Both fine and coarse aerosols have the same level of volume concentrations, although the mean effective radius of fine aerosol is an order of magnitude smaller than the coarse one. The mean effective radius and volume concentrations of the all modes are 0.34μm and 0.24 $\mu m^3/cm^3$, respectively, all peaking in spring. It's well known that the seasonality of the radius are anti-correlated well with the AEs.

The mean DRFs are -10.69, -16.45, 5.76 W/m^2 at TOA and -25.54, -21.37 and -8.38 W/m^2 at the surface for the total, scattering and absorbing aerosols, respectively, in clear sky condition. The fine mode DRFs at TOA are nearly an order of magnitude larger than the coarse ones for scattering aerosols while they have the same levels for absorbing aerosols. The DRFs estimated for urban Nanjing in this study are much stronger than those on the regional or global scales.

The seasonal variations of the DRFs, to some extent, are different between at TOA and the surface, between the scattering and absorbing aerosols, as well as between the fine and coarse modes. In clear sky condition, both the TOA and surface DRFs of scattering and absorbing aerosols are all the strongest

706 in summer for fine mode and in spring for coarse one. However, the largest DRF value appears in
707 spring for total scattering aerosols whereas in spring for total absorbing aerosols due to different fine
708 mode fractions of these two types of aerosols in different seasons, which further results in the strongest
709 (weakest) DRFs of all aerosols found in winter (spring) at the TOA and in summer (fall) at the surface
710 due to different fractions of scattering aerosols to the total aerosols.

711 The sensitivity of aerosol DRFs on the aerosol profiles is not significant in clear sky condition,
712 and the bias is about 5% for the TOA DRFs of absorbing aerosol while less 2% for the rest DRFs.
713 Overall, both scattering and absorbing aerosol DRFs at TOA would become weaker to some extent if
714 more aerosols were concentrated in lower layers of atmosphere or within boundary layer, especially for
715 absorption.

716

717 **Acknowledgements:** This work was supported by the National Key Basic Research Development
718 Program of China (2014CB441203, 2016YFC0203303), the National Natural Science Foundation of
719 China (41675143, 91544230, 41621005), the New Teachers' Fund for Postdoctoral Fellows, Ministry
720 of Education (20120091120031), FP7 project: REQUA (PIRSES-GA-2013-612671), and a project
721 Funded by the Priority Academic Program Development of the Jiangsu Higher Education Institutions
722 (PAPD). The authors would like to thank all members in the AERC of Nanjing University for
723 maintaining instruments.

724

725 **5 References**

726 Alam, K., Trautmann, T., and Blaschke, T.: Aerosol optical properties and radiative forcing over
727 mega-city Karachi. Atmos. Res. 101, 773-782, 2011.

728 Angström, A.: On the atmospheric transmission of sun radiation and on dust in the air, Geogr. Ann., 11,
729 156–166, 1929.
730 Arnott, W. P., Hamasha, K., Moosmuller, H., Sheridan, P. J., and Ogren, J. A.: Towards aerosol
731 light-absorption measurements with a 7-wavelength aethalometer: evaluation with a photoacoustic
732 instrument and 3-wavelength nephelometer, Aerosol Sci. Tech., 39, 17–29,
733 doi:10.1080/027868290901972, 2005.
734 Bellouin, N., Boucher, O., Tanré, D., and Dubovik, O.: Aerosol absorption over the clear-sky oceans
735 deduced from POLDER-1 and AERONET observations, Geophys. Res. Lett., 30, 1748,
736 doi:10.1029/2003GL017121, 2003.
737 Bergin, M. H., Cass, G. R., Xu, J., Fang, C., Zeng, L., Yu, T., Salmon, L. G., Kiang, C. S., Tang, X. Y.,
738 Zhang, Y. H., and Chameides, W. L.: Aerosol radiative, physical, and chemical properties in Beijing
739 during June 1999, J. Geophys. Res., 106 (D16), 17969–17980, 2001.
740 Cai, H. K., Zhou, R. J., Fu, Y. F., Zheng, Y. Y., and Wang, Y. J.: Cloud-aerosol lidar with or thogonal
741 polarization detection of aerosol optical properties after a crop burning case, Clim. Environ. Res.,
742 16, 469–478, 2011.
743 Che, H. Z., Zhang, X. Y., Xia, X., Goloub, P., Holben, B., Zhao, H., Wang, Y., Zhang, X. C., Wang, H.,
744 Blarel, L., Damiri, B., Zhang, R., Deng, X., Ma, Y., Wang, T., Geng, F., Qi, B., Zhu, J., Yu, J., Chen,
745 Q., and Shi, G.: Ground-based aerosol climatology of China: aerosol optical depths from the China
746 Aerosol Remote Sensing Network (CARSNET) 2002–2013, Atmos. Chem. Phys., 15, 7619–7652,
747 2015a.
748 Che, H. Z., Zhao, H. J., Wu, Y. F., Xia, X. A., Zhu, J., Wang, H., Wang, Y. Q., Sun, J. Y., Yu, J., Zhang,
749 X. Y., and Shi, G. Y.: Analyses of aerosol optical properties and direct radiative forcing over urban

and industrial regions in Northeast China, Meteorology and Atmospheric Physics, 127(3), 345-354, doi:10.1007/s00703-015-0367-3, 2015c.

Che, H., Wang, Y., and Sun, J.: Aerosol optical properties at Mt. Waliguan observatory, China, Atmos. Environ., 45, 6004–6009, 2011.

Che, H., Xia, X., Zhu, J., Li, Z., Dubovik, O., Holben, B., Goloub, P., Chen, H., Estelles, V., Cuevas-Agulló, E., Blarel, L., Wang, H., Zhao, H., Zhang, X., Wang, Y., Sun, J., Tao, R., Zhang, X., and Shi, G.: Column aerosol optical properties and aerosol radiative forcing during a serious haze-fog month over North China Plain in 2013 based on ground-based sunphotometer measurements, Atmos. Chem. Phys., 14, 2125–2138, doi:10.5194/acp-14-2125-2014, 2014.

Che, H., Xia, X., Zhu, J., Wang, H., Wang, Y., Sun, J., Zhang, X., and Shi, G.: Aerosol optical properties under the condition of heavy haze over an urban site of Beijing, China, Environ. Sci. Pollut. R., 22, 1043–1053, doi:10.1007/s11356-014-3415-5, 2015b.

Che, H.,Wang, Y., Sun, J., Zhang, X., Zhang, X., and Guo, J.: Variation of Aerosol Optical Properties over the Taklimakan Desert in China, Aerosol Air Qual. Res., 13, 777–785, 2013.

Chiang, C. W., Chen, W. N., Liang, W. A., Das, S. K., and Nee, J. B.: Optical properties of tropospheric aerosols based on measurements of lidar, sun-photometer, and visibility at Chung-Li (25°N, 121°E), Atmos. Environ., 41, 4128-4137, doi:10.1016/j.atmosenv.2007.01.019, 2007.

Dubovik, O. and King, M. D.: A flexible inversion algorithm for the retrieval of aerosol optical properties from Sun and sky radiance measurements, J. Geophys. Res., 105, 20673–20696, doi:10.1029/2000JD900282, 2000.

Dubovik, O., Sinyuk, A., Lapyonok, T., Holben, B. N., Mishchenko, M., Yang, P., Eck, T. F., Volten, H., Munoz, O., Veihelmann, B., van der Zande, W. J., Leon, J. F., Sorokin, M., and Slutsker, I.:

772 Application of spheroid models to account for aerosol particle nonsphericity in remote sensing of
773 desert dust, J. Geophys. Res.-Atmos., 111, D11208, doi:10.1029/2005jd006619, 2006.
774 Fan, X. H., Chen, H. B., Xia, X. A., Li, Z. Q., and Cribb, M.: Aerosol optical properties from the
775 Atmospheric Radiation Measurement Mobile Facility at Shouxian. China, J. Geophys. Res., 115,
776 D00K33, doi:10.1029/2010JD014650, 2010.
777 Forster, P., Ramaswamy, V., Artaxo, P., Berntsen, T., Betts, R., Fahey, D. W., Haywood, J., Lean, J.,
778 Lowe, D. C., Myhre, G., Nganga, J., Prinn, R., Raga, G., Schulz, M., and Van Dorland, R.: Changes
779 in atmospheric constituents and in radiative forcing, in: Climate Change 2007: The Physical
780 Science Basis. Contribution of Working Group I to the Fourth Assessment Report of the
781 Intergovernmental Panel on Climate Change, edited by: Solomon, S. et al., Cambridge Univ. Press,
782 Cambridge, UK, 129–234, 2007.
783 Hansen, A. D. A., Rosen, H., and Novakov, T.: The aethalometer: an instrument for the real time
784 measurements of optical absorption by aerosol particles, Sci. Total Environ., 36, 191–196, 1984.
785 He, X., Li, C. C., Lau, A. K. H., Deng, Z. Z., Mao, J. T., Wang, M. H., and Liu, X. Y.: An intensive
786 study of aerosol optical properties in Beijing urban area, Atmos. Chem. Phys., 9, 8903–8915,
787 doi:10.5194/acp-9-8903-2009, 2009.
788 Holben, B. N., Eck, T. F., Slutsker, I., Tanre, D., Buis, J. P., Setzer, A., Vermote, E., Reagan, J. A.,
789 Kaufman, Y. J., Nakajima, T., Lavenu, F., Jankowiak, I., and Smirnov, A.: AERONET-a federated
790 instrument network and data archive for aerosol characterization, Remote Sens. Environ., 66, 1-16,
791 1998.
792 Holler, R., Ito, K., Tohno, S., and Kasahara, M.: Wavelength-dependent aerosol single scattering albedo:
793 measurements and model calculations for a coastal site near the sea of Japan during ACE-Asia, J.

794 Geophys. Res., 108, 8648, doi:10.1029/2002JD003250, 2003.

795 Jacobson, M. Z.: A physically based treatment of elemental carbon optics: implication for global direct
796 forcing of aerosols, Geophys. Res. Lett., 27, 217-220, 2000.

797 Jacobson, M. Z.: Control of fossil-fuel particulate black carbon and organic matter, possibly the most
798 effective method of slowing global warming, J. Geophys. Res., 107, 4410,
799 doi:10.1029/2001JD001376, 2002.

800 Khatri, P., Ishizaka, Y., and Takamura, T.: A study on aerosol optical properties in an urban atmosphere
801 of Nagoya, Japan. J. Meteorol. Soc. Jpn., 87 (1), 19-38, 2009.

802 Kiehl, J. T. and Briegleb, B. P.: The relative roles of sulfate aerosols and greenhouse gases in climate
803 forcing, Science, 260, 311–314, 1993.

804 Kuhlmann, J., and Quaas, J.: How can aerosols affect the Asian summer monsoon? Assessment during
805 three consecutive pre-monsoon seasons from CALIPSO satellite data, Atmos. Chem. Phys., 10,
806 4673-4688, doi:10.5194/acp-10-4673-2010, 2010.

807 Li, J., Carlson, B. E., and Lacis, A. A.: Using single-scattering albedo spectral curvature to characterize
808 East Asian aerosol mixtures, J. Geophys. Res. Atmos., 120, 2037–2052, 2015c.

809 Li, J., Wang, W.-C., Liao, H., and Chang, W. Y.: Past and future direct radiative forcing of nitrate
810 aerosol in East Asia, Theor. Appl. Climatol., 121, 445–458, 2015b.

811 Li, S., Wang, T. J., Xie, M., Han, Y., and Zhuang, B. L.: Observed aerosol optical depth and angstrom
812 exponent in urban area of Nanjing, China, Atmos. Environ., 123, 350-356,
813 doi:10.1016/j.atmosenv.2015.02.048, 2015a.

814 Liao, H. and Seinfeld, J. H.: Global impacts of gas-phase chemistry-aerosol interactions on direct
815 radiative forcing by anthropogenic aerosols and ozone, J. Geophys. Res., 110, D18208,

doi:10.1029/2005JD005907, 2005.

Ma, X., and Yu, F.: Effect of spectral dependent surface albedo on Saharan dust direct radiative forcing. Geophys. Res. Lett. 39, L09808, 2012.

Madronich, S.: UV radiation in the natural and perturbed atmosphere, In: Tevini,M. (Ed.), UV-B Radiation and Ozone Depletion, Effects on Humans, Animals, Plants, Microorganisms, and Materials, Lewis Publisher, Boca Raton, pp. 17-69, 1993.

Markowicz, K. M., Flatau, P. J., Remiszewska, J., Witek, M., Reid, E. A., Reid, J. S., Bucholtz, Z., and Hilben, B.: Observations and modeling of the surface aerosol radiative forcing during UAE. J. Atmos. Sci. 65, 2877-2891, 2008.

Menon, S., Hansen, J., Nazarenko, L., and Luo, Y. F.: Climate effects of black carbon aerosols in China and India, Science, 297, 2250–2253, doi:10.1126/science.1075159, 2002.

Palancar, G.G., and Toselli, B. M.: Effects of meteorology and tropospheric aerosols on UV-B radiation: a 4-year study. Atmos. Environ. 18, 2749-2757, 2004.

Pan, L, Che, H. Z., Geng, F. H., Xia, X. A., Wang, Y. Q., Zhu, C. Z., Chen, M., Gao, W., and Guo, J. P.: Aerosol optical properties based on ground measurements over the Chinese Yangtze Delta Region, Atmos. Environ., 44, 2587-2596, doi:10.1016/j.atmosenv.2010.04.013, 2010.

Penner, J. E., Andreae, M., Annegarn, H., Barrie, L., Feichter, J., Hegg, D., Jayaraman, A., Leaitch, R., Murphy, D., Nganga, J., and Pitari, G.: Aerosols, their direct and indirect effects, in: Climate Change 2001: The Scientific Basis. Contribution of Working Group I to the Third Assessment Report of the Intergovernmental Panel on Climate Change, edited by: Houghton, J. T. et al., Cambridge University Press, Cambridge, UK and New York, NY, USA, 289–348, 2001.

Podgorny, I. A., and Ramanathan, V.: A modeling study of the direct effect of aerosols over the

tropical Indian Ocean, J Geophys. Res. 106, D20, 24097–24105, 2001.

Qi, B., Hu, D. Y., Che, H. Z., Du, R. G., Wu, Y. F., Xia, X. A., Zha, B., Liu, J., Niu, Y. W., Wang, H., Zhang, X. Y., and Shi, G. Y.: Seasonal variation of aerosol optical properties in an urban site of the Yangtze Delta Region of China. Aerosol Air Qual. Res., 16, 2884-2896, 2016.

Reddy, M. S., Boucher, O., Bellouin, N., Schulz, M., Balkanski, Y., Dufresne, J. L., and Pham, M.: Estimates of global multicomponent aerosol optical depth and direct radiative perturbation in the Laboratoire de Meteorologie Dynamique general circulation model, J. Geophys. Res., 110, D10S16, doi:10.1029/2004JD004757, 2005.

Russell, P. B., Kacenelenbogen, M., Livingston, J. M., Hasekamp, O. P., Burton, S. P., Schuster, G. L., Johnson, M. S., Knobelspiesse, K. D., Redemann, J., Ramachandran, S., and Holben, B.: A multiparameter aerosol classification method and its application to retrievals from spaceborne polarimetry, J. Geophys. Res.-Atmos., 119, 9838–9863, doi:10.1002/2013JD021411, 2014.

Sun, H., Pan, Z., and Liu, X.: Numerical simulation of spatial-temporal distribution of dust aerosol and its direct radiative effects on East Asian climate, J. Geophys. Res., 117, D13206, doi:10.1029/2011JD017219, 2012.

Tao, R., Che, H. Z., Chen, Q. L., Tao, J., Wang, Y. Q., Sun, J. Y., Wang, H., and Zhang, X. X.: Study of aerosol optical properties based on ground measurements over Sichuan Basin, China, Aerosol and Air Quality Research, 14: 905–915. doi:10.4209/aaqr.2012.07.0200, 2014.

Wang, T. J., Zhuang, B. L., Li, S., Liu, J., Xie, M., Yin, C. Q., Zhang, Y., Yuan, C., Zhu, J. L., Ji, L. Q., and Han, Y.: The interactions between anthropogenic aerosols and the East Asian summer monsoon using RegCCMS, J. Geophys. Res. Atmos., 120, doi:10.1002/2014JD022877, 2015.

Wang, Y., Che, H. Z., Ma, J. Z., Wang, Q., Shi, G. Y., Chen, H. B., Goloub, P., and Hao, X. J.: Aerosol

860 radiative forcing under clear, hazy, foggy, and dusty weather conditions over Beijing, China,
861 Geophys. Res. Lett., 36, L06804, doi:10.1029/2009GL037181, 2009.
862 Weingartner, E., Saathoff, H., Schnaiter, M., Streit, N., Bitnar, B., and Baltensperger, U.: Absorption of
863 light by soot particles: determination of the absorption coefficient by means of aethalometers, J.
864 Aerosol Sci., 34, 1445–1463, doi:10.1016/S0021-8502(03)00359-8, 2003.
865 Wu, Y. F., Zhang, R. J., Pu, Y. F., Zhang, L. M., Ho, K. F., and Fu, C. B.: Aerosol optical properties
866 observed at a semi-arid rural site in northeastern China, Aerosol Air Qual. Res., 12, 503–514, 2012.
867 Xia, X. A., Li, Z. Q., Holben, B., Wang, P., Eck, T., Chen, H. B., Cribb, M., and Zhao, Y. X.: Aerosol
868 optical properties and radiative effects in the Yangtze Delta region of China, J. Geophys. Res., 112,
869 D22S12, doi:10.1029/2007JD008859, 2007.
870 Xia, X., Che, H., Zhu, J., Chen, H., Cong, Z., Deng, X., Fan, X., Fu, Y., Goloub, P., Jiang, H., Liu, Q.,
871 Mai, B., Wang, P., Wu, Y., Zhang, J., Zhang, R., and Zhang, X.: Ground-based remote sensing of
872 aerosol climatology in China: aerosol optical properties, direct radiative effect and is
873 parameterization, Atmos. Environ., 214, 243-251, doi:10.1016/j.atmosenv.2015.06.071, 2016.
874 Xu, J., Bergin, M. H., Greenwald, R., Schauer, J. J., Shafer, M. M., Jaffrezo, J. L., and Aymoz, G.:
875 Aerosol chemical, physical, and radiative characteristics near a desert source region of Northwest
876 China during ACE-Asia, J. Geophys. Res., 109, D19S03, doi:10.1029/2003JD004239, 2004.
877 Xu, J., Bergin, M. H., Yu, X., Liu, G., Zhao, J., Carrico, C. M., and Baumann, K.: Measurement of
878 aerosol chemical, physical and radiative properties in the Yangtze delta region of China, Atmos.
879 Environ., 36, 161–173, 2002.
880 Xu, J., Tao, J., Zhang, R., Cheng, T., Leng, C., Chen, J., Huang, G., Li, X., and Zhu, Z.: Measurements
881 of surface aerosol optical properties in winter of Shanghai, Atmos. Res., 109-110, 25–35, 2012.

882 Yan, P., Tang, J., Huang, J., Mao, J. T., Zhou, X.J., Liu, Q., Wang, Z. F., and Zhou, H. G.: The
883 measurement of aerosol optical properties at a rural site in Northern China, Atmos. Chem. Phys., 8,
884 2229–2242, doi:10.5194/acp-8-2229-2008, 2008.
885 Yu, J., Che, H. Z., Chen, Q. L., Xia, X. A., Zhao, H. J., Wang, H., Wang, Y. Q., Zhang, X. X., and Shi,
886 G. Y.: Investigation of aerosol optical depth (AOD) and Ångström exponent over the desert region
887 of northwestern China based on measurements from the China Aerosol Remote Sensing Network
888 (CARSNET), Aerosol Air Qual. Res., 15, 2024-2036, doi:10.4209/aaqr.2014.12.0326, 2015.
889 Yu, X. N., Ma, J., Kumar, K. R., Zhu, B., An, J. L., He, J. Q., and Li, M.: Measurement and analysis of
890 surface aerosol optical properties over urban Nanjing in the Chinese Yangtze River Delta, Sci. Total
891 Environ., 542, 277-291, 2016.
892 Yu, X. N., Zhu, B., Yin, Y., Fan, S. X., and Chen, A. J.: Seasonal variation of columnar aerosol optical
893 properties in Yangtze River Delta in China, Adv. Atmos. Sci., 28(6), 1326-1335,
894 doi:10.1007/s00376-011-0158-9, 2011.
895 Zhang, L., Sun, J. Y., Shen, X. J., Zhang, Y. M., Che, H., Ma, L. Q., Zhang, Y. W., Zhang, X. Y., and
896 Ogren, J. A.: Observations of relative humidity effects on aerosol light scattering in the Yangtze
897 River Delta of China, Atmos. Chem. Phys., 15, 8439–8454, 2015.
898 Zhang, Q., Streets, D. G., Carmichael, G. R., He, K. B., Huo, H., Kannari, A., Klimont, Z., Park, I. S.,
899 Reddy, S., Fu, J. S., Chen, D., Duan, L., Lei, Y., Wang, L. T., and Yao, Z. L.: Asian emissions in
900 2006 for the NASA INTEX-B mission, Atmos. Chem. Phys., 9, 5131–5153,
901 doi:10.5194/acp-9-5131-2009, 2009.
902 Zhang, W., Hu, B., Chen, C. H., Du, P., Zhang, L., and Feng, G. H.: Scattering properties of
903 atmospheric aerosols over Lanzhou City and applications using an integrating nephelometer, Adv.

904 Atmos. Sci., 21(6), 848–856, 2004.

905 Zhang, X. Y., Wang, Y. Q., Niu, T., Zhang, X. C., Gong, S. L., Zhang, Y. M., and Sun, J. Y.:
906 Atmospheric aerosol compositions in China: Spatial/temporal variability, chemical signature,
907 regional haze distribution and comparisons with global aerosols, Atmos. Chem. Phys., 12, 779–799,
908 doi:10.5194/acp-12-779-2012, 2012.

909 Zhao, H. J., Che, H. Z., Zhang, X. Y., Ma, Y. J., Wang, Y. F., Wang, X. X., Liu, C., Hou, B., and Che,
910 X. C.: Aerosol optical properties over urban and industrial region of Northeast China by using
911 ground-based sun-photometer Measurement, Atmos. Environ., 75, 270-278.
912 doi:10.1016/j.atmosenv.2013.04.048, 2013.

913 Zheng, Y., Che, H. Z., Zhao, T. L., Xia, X. A., Gui, K., An, L. C., Qi, B., Wang, H., Wang, Y. Q., Yu, J.,
914 and Zhang, X. Y.: Aerosol optical properties during the World Athletics Championships and Victory
915 Day Military Parade over Beijing in August and September 2015, Atmosphere, 7(3), 47;
916 doi:10.3390/ atmos7030047, 2016.

917 Zhu, J., Che, H. Z., Xia, X. A., Chen, H. B., Goloub, P., and Zhang, W. X.: Column-integrated aerosol
918 optical and physical properties at a regional background atmosphere in North China Plain, Atmos.
919 Environ., 84, 54-64, doi:10.1016/j.atmosenv.2013.11.019, 2014.

920 Zhu, J., Wang, T., Talbot, R., Mao, H., Hall, C. B., Yang, X., Fu, C., Zhuang, B., Li, S., Han, Y., and
921 Huang, X.: Characteristics of atmospheric Total Gaseous Mercury (TGM) observed in urban
922 Nanjing, China, Atmos. Chem. Phys., 12, 12103–12118, doi:10.5194/acp-12-12103-2012, 2012.

923 Zhuang, B. L., Li, S., Wang, T. J., Deng, J. J., Xie, M., Yin, C. Q., and Zhu, J. L.: Direct radiative
924 forcing and climate effects of anthropogenic aerosols with different mixing states over China,
925 Atmos. Environ., 79, 349–361, doi:10.1016/j.atmosenv.2013.07.004, 2013a.

926 Zhuang, B. L., Liu, Q., Wang, T. J., Yin, C. Q., Li, S., Xie, M., Jiang, F., and Mao, H. T.: Investigation
927 on semi-direct and indirect climate effects of fossil fuel black carbon aerosol over China, Theor.
928 Appl. Climatol., 114, 651–672, doi:10.1007/s00704-013-0862-8, 2013b.
929 Zhuang, B. L., Wang, T. J., Li, S., Liu, J., Talbot, R., Mao, H. T., Yang, X. Q., Fu, C. B., Yin, C. Q.,
930 Zhu, J. L., Che, H. Z., and Zhang, X. Y.: Optical properties and radiative forcing of urban aerosols
931 in Nanjing, China, Atmos. Environ., 83, 43–52, 2014a.
932 Zhuang, B. L., Wang, T. J., Liu, J., Li, S., Xie, M., Yang, X. Q., Fu, C. B., Sun, J. N., Yin, C. Q., Liao, J.
933 B., Zhu, J. L., and Zhang, Y.: Continuous measurement of black carbon aerosol in urban Nanjing of
934 Yangtze River Delta, China, Atmos. Environ., 89, 415–424, 2014b.
935 Zhuang, B. L., Wang, T. J., Liu, J., Ma, Y., Yin, C. Q., Li, S., Xie, M., Han, Y., Zhu, J. L., Yang, X. Q.,
936 and Fu, C. B.: Absorption coefficient of urban aerosol in Nanjing, west Yangtze River Delta, China,
937 Atmos. Chem. Phys., 15, 13633–13646, 2015.

938

939 **Figure captions:**

940 Figure 1. Monthly variations of the total (a), scattering (b), and absorbing (c) aerosol optical depths
941 (AOD) at 550 nm, including the ratio of the AOD in fine or coarse mode to the AOD in all mode (line
942 with triangle markers in green) in urban area of Nanjing. The 10th, 25th, median, 75th, 90th percentile
943 values of the all mode AOD are presented as box plots. The monthly means of the all mode AODs are
944 presented as cycle markers in gray.

945 Figure 2. Monthly variations of the total (a), scattering (b), and absorbing aerosol (c) Ångström
946 exponents (AE) at 440/870 nm for the all, fine and coarse modes in urban area of Nanjing.

947 Figure 3. Monthly variations of the all, fine, and coarse mode aerosol single scattering albedo (SSA) at

550 nm (a) and the aerosol refractive indices at 440 nm (b) in urban area of Nanjing.

Figure 4. Frequency distributions of the total (a), scattering (b), and absorbing aerosol (c) AODs at 550 nm for the all (AOD, SAOD, AAOD), fine (FAOD, FSAOD, FAAOD) and coarse (CAOD, CSAOD, CAAOD) modes in urban area of Nanjing.

Figure 5. Frequency distributions of the total (a), scattering (b), and absorbing aerosol (c) AEs at 440/870 nm for the all (AE, SAE, AAE), fine (FAE, FSAE, FAAE) and coarse (CAE, CSAE, CAAE) modes in urban area of Nanjing.

Figure 6. Frequency distributions of the all (SSA), fine (FSSA), and coarse (CSSA) mode aerosol SSAs at 550 nm (a) and the real and imaginary parts at 440 nm (b) in urban Nanjing.

Figure 7. Comparisons between CE-318 and MODIS based AOD at 550 nm and between AE at 440/870 nm for CE-318 and at 412/470 nm for MODIS in Nanjing.

Figure 8. Comparisons between the absorbing aerosol optical depth (AAOD) at 550 nm from CE-318 and surface absorption coefficient (AAC) at 520 nm from AE-31 (a) and between the column AAE at 440/870 nm from CE-318 and surface AAE at 470/880 nm from AE-31 (b) in urban Nanjing.

Figure 9. The averaged aerosol volume size ($\mu m^3/\mu m^2$) distributions in different seasons (a) and in different AOD levels in urban Nanjing.

Figure 10. Seasonal variations of the effective (a, μm) and mean (b, μm) radius of aerosols as well as the aerosol volume concentrations (c, $\mu m^3/cm^3$) in the all, fine and coarse modes in urban Nanjing.

Figure 11. Relationships between the monthly mean values of 491 nm SSA and total Ångström exponent (AE) at 491/870 nm (a), between the monthly mean values of the real refractive index at 670 nm and AE at 491/870 nm (b), and between the monthly mean values of the SSA difference (870–491 nm) and AE at 491/870 nm (c).

970 Figure 12. Distribution of the SSA and AAOD Curvatures in urban area of Nanjing under different
971 spectral SSA conditions, including monotonically decreasing, increasing SSA spectra and peaked SSA
972 spectra.

973 Figure 13. The aerosol vertical proportions (%) from CALIPSO, Polarization-Raman Lidar and their
974 average in Nanjing.

975 Figure 14. Seasonal variations of the clear sky aerosol direct radiative forcing (DRF, W/m^2) at both
976 TOA (a~c) and the surface (d~f). The DRFs of the total (a, d), scattering (b, e) and absorbing (c, f)
977 aerosols in the all, fine and coarse modes are all investigated in urban Nanjing.

978 Figure 15. Comparisons in the absorbing aerosol DRFs (W/m^2) between from BC SSA and from the
979 total aerosol DRF minus the scattering one.

980 Figure 16. Sensitivities of the TOA and the surface aerosol DRFs (day time, W/m^2) to the different
981 aerosol profiles in clear conditions, for the total, scattering and absorbing aerosols.

982

983 **Tables:**

984 Table 1 Statistical summary of the columnar aerosol optical properties in urban area of Nanjing

Factors	Max	Min	Mean±SD	Meadian
550 nm AOD	2.3208	0.2723	0.6494±0.2852	0.5912
550 nm FAOD	2.2216	0.1468	0.5257±0.2806	0.4479
550 nm CAOD	0.9891	0.0139	0.1237±0.1076	0.0858
550 nm SAOD	2.2744	0.2443	0.6059±0.2747	0.5492
550 nm FSAOD	2.1459	0.1435	0.5014±0.2713	0.4263
550 nm CSAOD	0.8842	0.0113	0.1045±0.0957	0.0705
550 nm AAOD	0.2304	0.0020	0.0435±0.0240	0.0421
550 nm FAAOD	0.1424	0.0005	0.0244±0.0175	0.0208
550 nm CAAOD	0.1163	0.0009	0.0192±0.0145	0.0156
440/870 nm AE	1.9100	0.3085	1.2045±0.2856	1.2436
440/870 nm FAE	2.3625	0.3565	1.7083±0.2979	1.7364
440/870 nm CAE	-0.0789	-0.3805	-0.1876±0.0430	-0.1898
440/870 nm SAE	1.9916	0.2958	1.1976±0.3085	1.2386
440/870 nm FSAE	2.3653	0.3463	1.7102±0.2980	1.7368
440/870 nm CSAE	-0.1048	-0.7111	-0.3838±0.1017	-0.3864
440/870 nm AAE	3.4619	0.1483	1.3237±0.4820	1.2587

440/870 nm FAAE	4.5118	0.2912	1.7521±0.6470	1.6516
440/870 nm CAAE	3.1264	-0.0844	0.8748±0.4589	0.8209
550 nm SSA	0.9959	0.8053	0.9297±0.0335	0.9305
550 nm FSSA	0.9974	0.8388	0.9524±0.0261	0.9549
550 nm CSSA	0.9835	0.5898	0.8208±0.0754	0.8225
440 nm Real part	1.6000	1.3300	1.4423±0.0638	1.4374
440 nm Imaginary part	0.0301	0.0005	0.0084±0.0047	0.0078

AOD: Aerosol optical depth
FAOD: Fine aerosol optical depth
CAOD: Coarse aerosol optical depth
SAOD: Scattering aerosol optical depth
FSAOD: Scattering aerosol optical depth in fine mode
CSAOD: Scattering aerosol optical depth in coarse mode
AAOD: Absorbing aerosol optical depth
FAAOD: Absorbing aerosol optical depth in fine mode
CAAOD: Absorbing aerosol optical depth in coarse mode
AE: Ångström exponent of total aerosols
FAE: Ångström exponent of fine aerosols
CAE: Ångström exponent of coarse aerosols
SAE: Ångström exponent of scattering aerosols
FSAE: Ångström exponent of scattering aerosols in fine mode
CSAE: Ångström exponent of scattering aerosols in coarse mode
AAE: Ångström exponent of absorbing aerosols
FAAE: Ångström exponent of absorbing aerosols in fine mode
CAAE: Ångström exponent of absorbing aerosols in coarse mode
SSA: Single scattering albedo of total aerosols
FSSA: Single scattering albedo of fine aerosols
CSSA: Single scattering albedo of coarse aerosols

Table 2 Seasonal mean±SD of the columnar aerosol optical properties in urban area of Nanjing

Factors	MAM	JJA	SON	DJF
550 nm AOD	0.6788±0.2919	0.7508±0.3749	0.5866±0.2447	0.6560±0.2976
550 nm FAOD	0.4739±0.2613	0.6798±0.3793	0.5149±0.2462	0.5687±0.2978
550 nm CAOD	0.2048±0.1356	0.0710±0.0599	0.0717±0.0346	0.0873±0.0685
550 nm SAOD	0.6284±0.2835	0.7031±0.3728	0.5495±0.2342	0.6157±0.2829
550 nm FSAOD	0.4529±0.2552	0.6463±0.3760	0.4901±0.2366	0.5428±0.2846
550 nm CSAOD	0.1756±0.1225	0.0568±0.0497	0.0593±0.0315	0.0728±0.0601
550 nm AAOD	0.0503±0.0208	0.0477±0.0307	0.0372±0.0200	0.0403±0.0271
550 nm FAAOD	0.0211±0.0125	0.0335±0.0212	0.0248±0.0157	0.0259±0.0211
550 nm CAAOD	0.0292±0.0165	0.0142±0.0137	0.0124±0.0066	0.0144±0.0111
440/870 nm AE	0.9915±0.2385	1.2174±0.2639	1.3744±0.1907	1.3134±0.2461
440/870 nm FAE	1.7474±0.2896	1.4701±0.3075	1.7408±0.2582	1.6935±0.3019
440/870 nm CAE	-0.1998±0.0352	-0.1699±0.0471	-0.1862±0.0424	-0.1807±0.0464
440/870 nm SAE	0.9812±0.2687	1.2733±0.2950	1.3824±0.2043	1.2956±0.2697
440/870 nm SFAE	1.7555±0.2862	1.5218±0.3397	1.7492±0.2545	1.6809±0.3039
440/870 nm SCAE	-0.3752±0.0743	-0.2815±0.0678	-0.3797±0.0991	-0.4016±0.1162
440/870 nm AAE	1.1885±0.4500	0.7971±0.2657	1.3290±0.4533	1.5007±0.4520
440/870 nm FAAE	1.7352±0.6059	0.9943±0.2672	1.6715±0.5970	1.8947±0.6545
440/870 nm CAAE	0.8542±0.4665	0.3771±0.2753	0.8312±0.4479	0.9798±0.4235
550 nm SSA	0.9204±0.0313	0.9241±0.0422	0.9348±0.0331	0.9378±0.0331

550 nm FSSA	0.9527±0.0237	0.9405±0.0356	0.9518±0.0253	0.9555±0.0265
550 nm CSSA	0.8340±0.0628	0.7868±0.0953	0.8115±0.0752	0.8211±0.0810
440 nm Real part	1.4647±0.0628	1.4075±0.0609	1.4252±0.0602	1.4404±0.0582
440 nm Imaginary part	0.0084±0.0040	0.0083±0.0052	0.0080±0.0044	0.0083±0.0053

Table 3. The annual mean aerosol direct radiative forcing (W/m^2) in urban area of Nanjing

Species	Clear sky	
	TOA	Surface
TA	-10.69±3.37	-25.54±2.83
FA	-11.17±3.09	-21.37±2.78
CA	-0.33±0.60	-6.15±2.90
SA	-16.45±2.81	-17.17±2.96
FSA	-15.08±3.18	-15.74±3.35
CSA	-2.31±1.18	-2.42±1.24
AA	5. 76±1.27	-8.38±1.56
FAA	3.91±0.95	-5.63±1.16
CAA	1.99±1.07	-3.73±1.71

TA: Total aerosols
FA: Fine aerosols
CA: Coarse aerosols
SA: All scattering aerosols
FSA: Scattering aerosols in fine mode
CSA: Scattering aerosols in coarse mode
AA: All absorbing aerosols' forcing
FAA: Fine absorbing aerosols' forcing
CAA: Coarse absorbing aerosols' forcing

Figures:

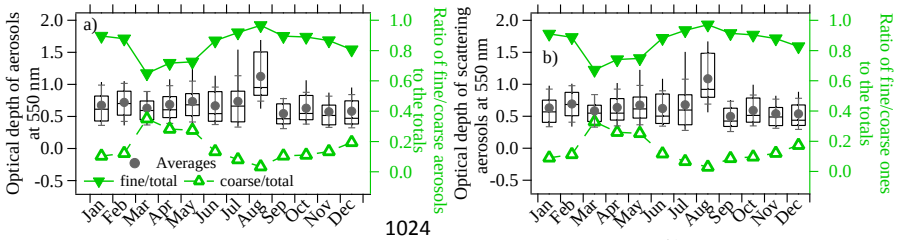

a) b)

Atmos. Chem. Phys. Discuss., https://doi.org/10.5194/acp-2017-215
Manuscript under review for journal Atmos. Chem. Phys.
Discussion started: 21 June 2017

Atmospheric Chemistry and Physics Discussions

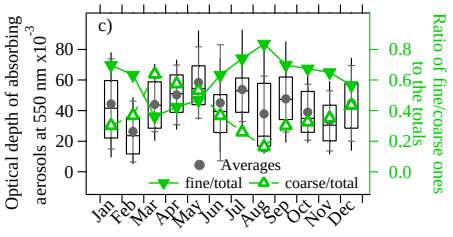

c)

Figure 1.

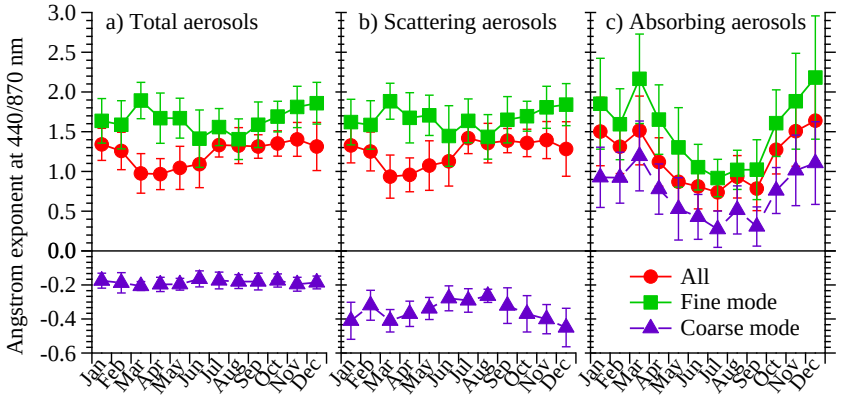

Figure 2.

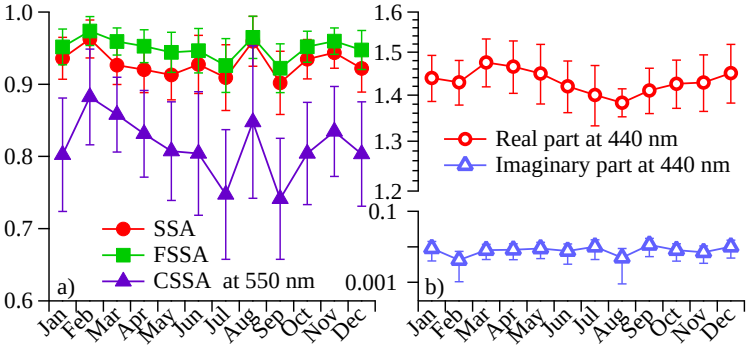

Figure 3

Atmos. Chem. Phys. Discuss., https://doi.org/10.5194/acp-2017-215
Manuscript under review for journal Atmos. Chem. Phys.
Discussion started: 21 June 2017

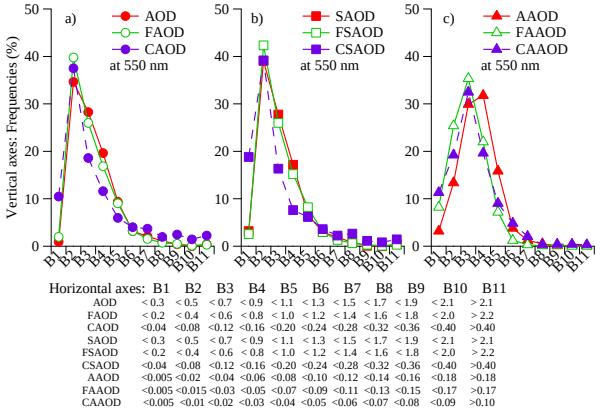

Figure 4

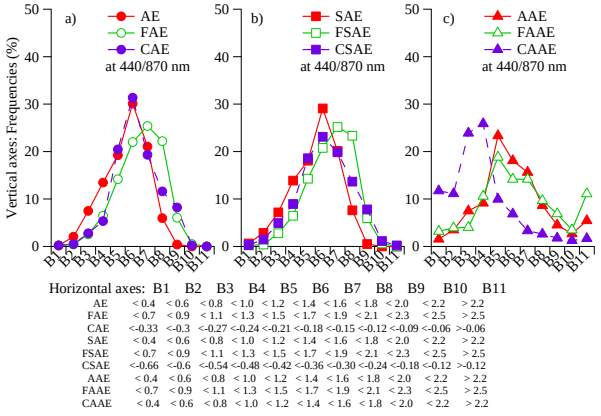

Figure 5

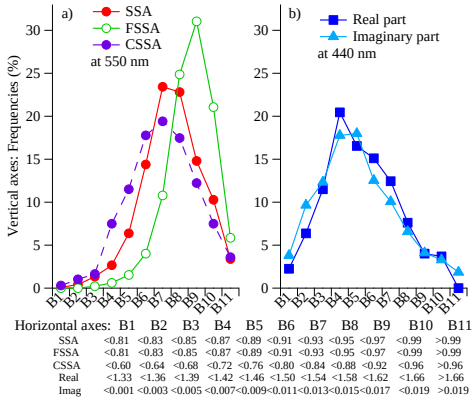

Figure 6

Atmos. Chem. Phys. Discuss., https://doi.org/10.5194/acp-2017-215
Manuscript under review for journal Atmos. Chem. Phys.
Discussion started: 21 June 2017

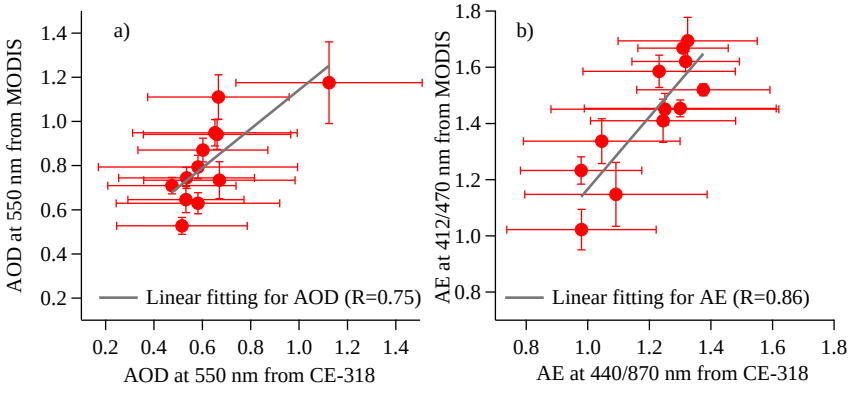

Figure 7

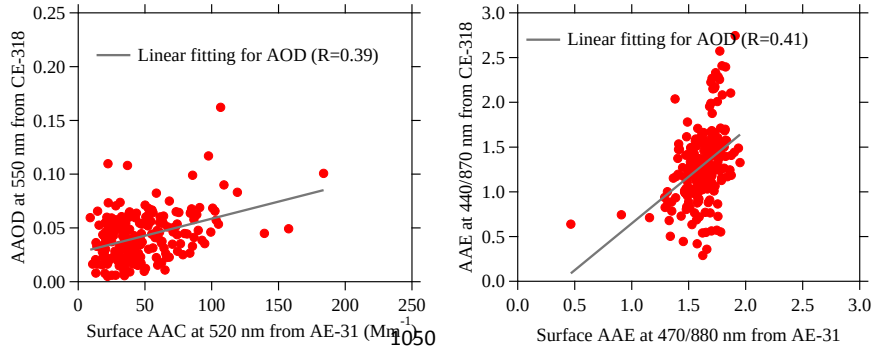

Figure 8

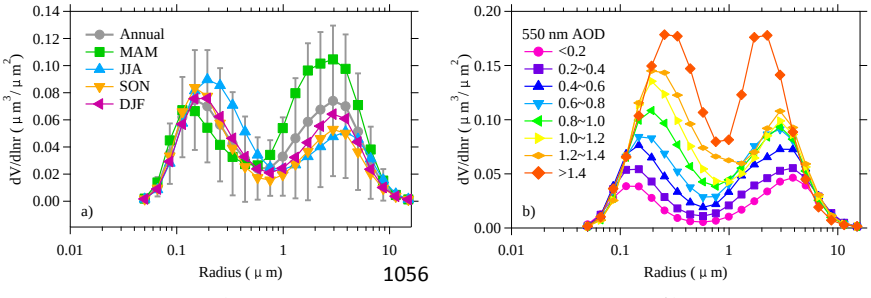

Figure 9

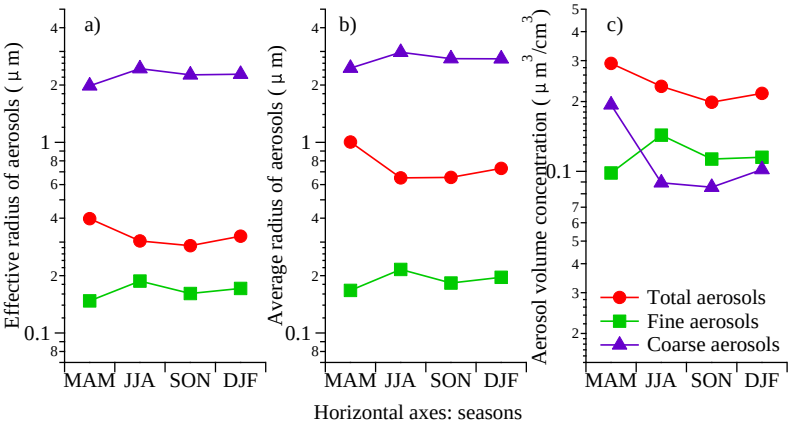

Figure 10

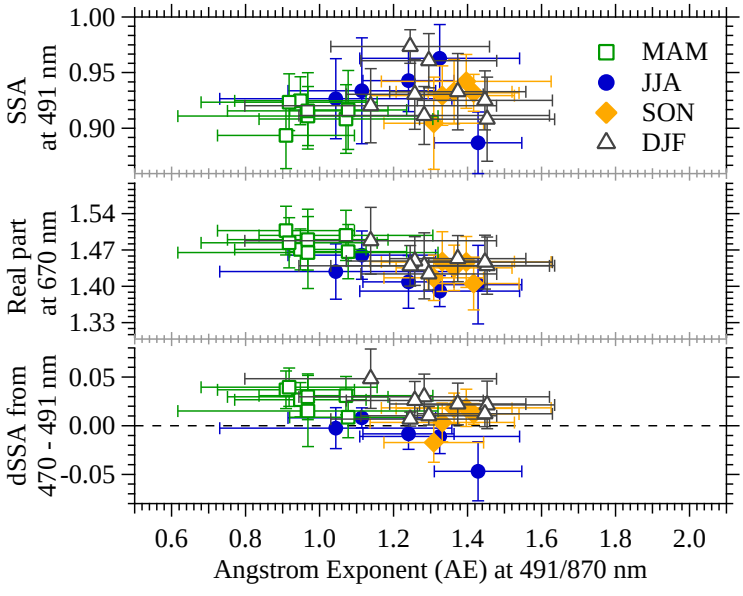

Figure 11

Atmos. Chem. Phys. Discuss., https://doi.org/10.5194/acp-2017-215
Manuscript under review for journal Atmos. Chem. Phys.
Discussion started: 21 June 2017

Atmospheric Chemistry and Physics Discussions

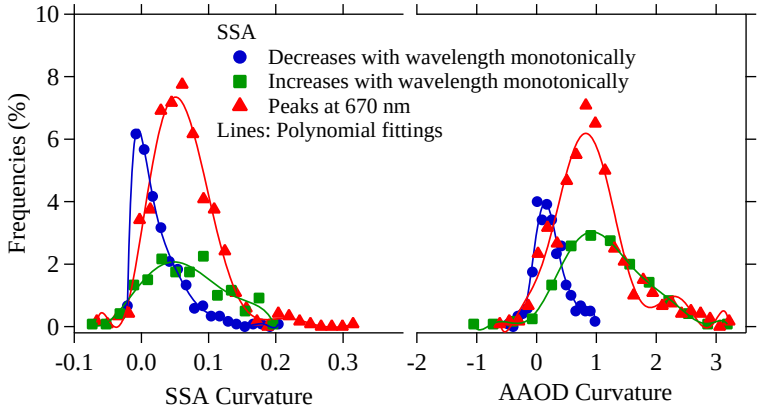

1066
1067 Figure 12
1068

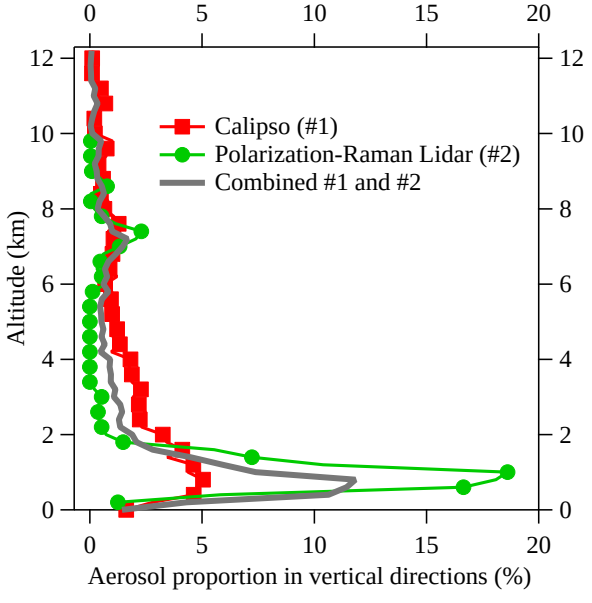

1069
1070 Figure 13
1071

Atmos. Chem. Phys. Discuss., https://doi.org/10.5194/acp-2017-215
Manuscript under review for journal Atmos. Chem. Phys.
Discussion started: 21 June 2017

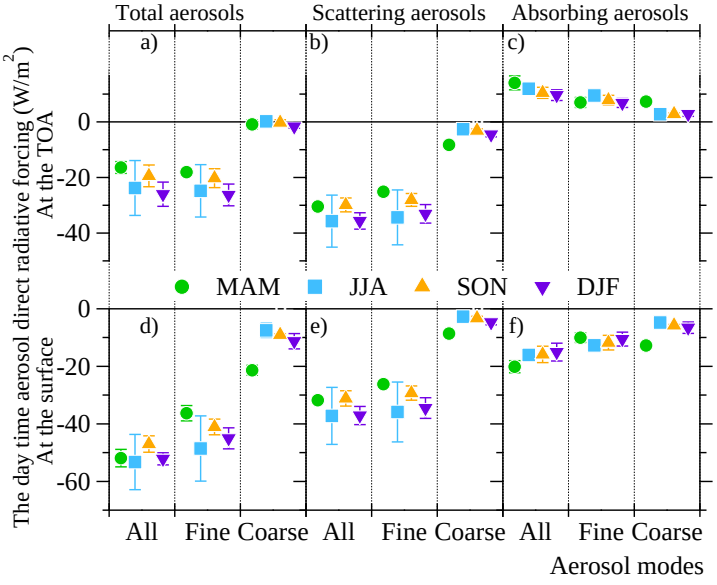

Figure 14

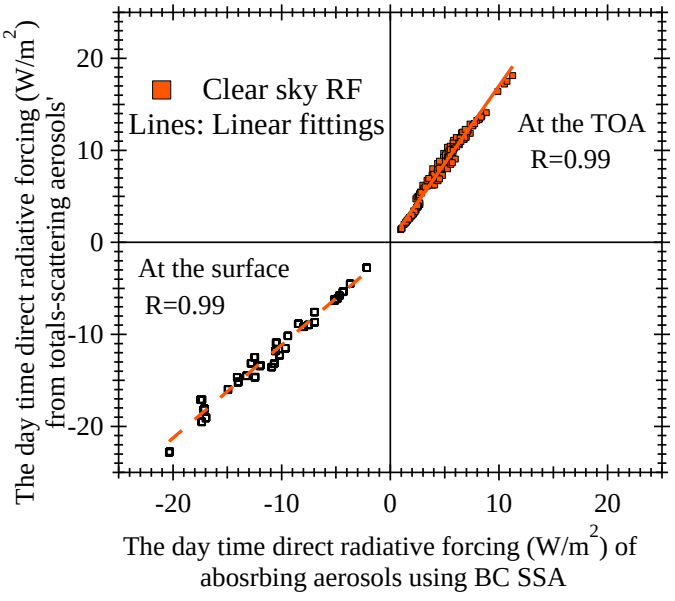

Figure 15

Atmos. Chem. Phys. Discuss., https://doi.org/10.5194/acp-2017-215
Manuscript under review for journal Atmos. Chem. Phys.
Discussion started: 21 June 2017

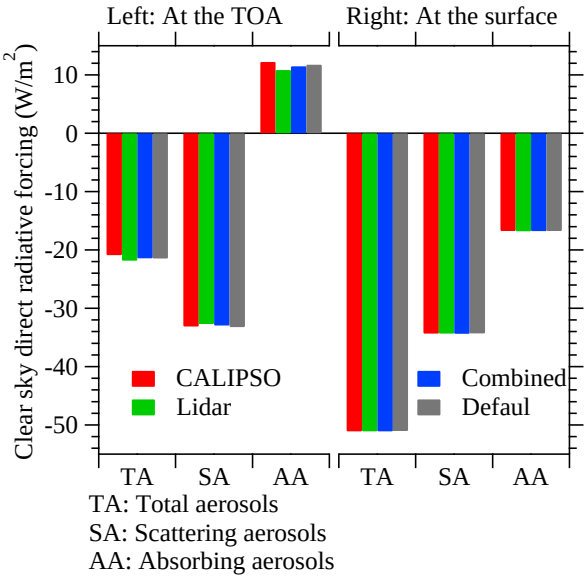

Figure 16